

ALGEBRAIC ORDER AND THE BKT TRANSITION IN AN  
EXCITON-POLARITON GAS

A DISSERTATION  
SUBMITTED TO THE DEPARTMENT OF APPLIED PHYSICS  
AND THE COMMITTEE ON GRADUATE STUDIES  
OF STANFORD UNIVERSITY  
IN PARTIAL FULFILLMENT OF THE REQUIREMENTS  
FOR THE DEGREE OF  
DOCTOR OF PHILOSOPHY

Wolfgang Hartmut Nitsche

June 2014

© 2014 by Wolfgang Hartmut Nitsche. All Rights Reserved.  
Re-distributed by Stanford University under license with the author.

This dissertation is online at: <http://purl.stanford.edu/by756rx2856>

I certify that I have read this dissertation and that, in my opinion, it is fully adequate in scope and quality as a dissertation for the degree of Doctor of Philosophy.

**Yoshihisa Yamamoto, Primary Adviser**

I certify that I have read this dissertation and that, in my opinion, it is fully adequate in scope and quality as a dissertation for the degree of Doctor of Philosophy.

**Hideo Mabuchi**

I certify that I have read this dissertation and that, in my opinion, it is fully adequate in scope and quality as a dissertation for the degree of Doctor of Philosophy.

**David Miller**

Approved for the Stanford University Committee on Graduate Studies.

**Patricia J. Gumport, Vice Provost for Graduate Education**

*This signature page was generated electronically upon submission of this dissertation in electronic format. An original signed hard copy of the signature page is on file in University Archives.*



# Abstract

Below a critical temperature, three-dimensional bosonic gases form a Bose-Einstein-condensate which exhibits spatial coherence. In two-dimensional (2D) systems, true long range order is impossible at non-zero temperatures since long-range fluctuations which increase the entropy and destroy the coherence can easily be excited. However it has been predicted by the Berezinskii-Kosterlitz-Thouless (BKT) theory that such a 2D condensate can exhibit quasi-long-range order which is characterized by a power-law decay of the spatial correlation function.

This thesis presents the first observation of the coherence decay in a 2D exciton-polariton condensate with a power-law whose exponent (less than  $1/4$ ) behaves as predicted by the theory.

Exciton-polaritons are quasi-particles which can be described as the quantum mechanical superposition of an exciton in a quantum well and a photon trapped in a semiconductor cavity. Due to their bosonic properties and small effective mass, they already condense at a temperature of a few kelvin, compared to a few hundred nanokelvin in the atomic case. Exciton-polaritons are created by optical excitation of the sample, and they continuously decay through the leakage of photons out of the sample. These leaking photons preserve the coherence properties of the decaying exciton-polaritons, and their coherence can be determined through interference measurements.



# Acknowledgement

I want to thank all those who helped with the research leading to this thesis

First and foremost I want to thank my adviser Professor Yoshihisa Yamamoto for accepting me into his group and giving me this research project. Especially I always appreciated his deep understanding of exciton-polariton physics and his helpful guidance of my research.

Next, I want to thank Professor Hideo Mabuchi and Professor David A. B. Miller for agreeing to be in my thesis reading committee, as well as Professor Mark Brongersma and Professor Alexander Fetter who served as the additional members in the committee for my oral defense.

I also want to thank the other members of the Yamamoto group for the friendly work environment: Na Young Kim who managed the exciton-polariton subgroup has always been available to give helpful advice and discuss the measurement plans and results, which I appreciated. Georgios Roumpos worked with me in the lab during the first year, and after his graduation I took over most of his setup.

The exciton-polariton sample for this thesis has been grown by Christian Schneider under the guidance of Professor Sven Höfling and Professor Alfred Forchel, for which I want to thank all of them.

Finally, I also want to acknowledge the Gerhard Casper Stanford Graduate Fellowship for providing most of my funding.



# Contents

Abstract	v
Acknowledgement	vii
<b>1 Exciton-polaritons</b>	<b>1</b>
1.1 Micro-cavity photons . . . . .	1
1.2 Quantum well excitons . . . . .	2
1.3 Coupling between photons and excitons . . . . .	2
1.3.1 Photon and exciton fraction . . . . .	5
1.3.2 Momentum dependence of the Hopfield coefficients . . . . .	6
1.3.3 Effective mass of exciton-polaritons . . . . .	8
1.3.4 Lifetime of exciton-polaritons . . . . .	8
1.3.5 Spin . . . . .	9
1.3.6 Condensation of exciton-polaritons . . . . .	10
<b>2 Superfluidity</b>	<b>11</b>
2.1 Landau's criterion . . . . .	11
2.1.1 Initially in $\mathbf{K}$ frame . . . . .	13
2.1.2 Initially in $\mathbf{K}'$ frame . . . . .	13
2.1.3 Final in $\mathbf{K}'$ frame . . . . .	14

2.1.4	Final in $\mathbf{K}$ frame . . . . .	14
2.1.5	Energy change . . . . .	15
2.2	Vortices . . . . .	16
2.2.1	Rotating a rigid object . . . . .	16
2.2.2	Impossibility to rotate a superfluid . . . . .	17
<b>3</b>	<b>Spatial coherence</b>	<b>19</b>
3.1	Correlation function . . . . .	19
3.2	Coherence of three dimensional condensates . . . . .	20
3.3	Coherence of two dimensional systems . . . . .	20
3.3.1	Lack of real long-range order . . . . .	20
3.3.2	Possibility of quasi-long-range order . . . . .	21
3.3.3	Decay mechanisms for spatial coherence . . . . .	21
3.3.4	Phononic phase fluctuations . . . . .	25
3.3.5	BKT transition . . . . .	26
<b>4</b>	<b>Sample</b>	<b>29</b>
4.1	Position dependent detuning . . . . .	31
4.2	Experimental characterization . . . . .	31
<b>5</b>	<b>Experimental setup</b>	<b>35</b>
5.1	Cryostat . . . . .	36
5.2	Optical pump (for creating exciton-polaritons) . . . . .	36
5.2.1	Laser . . . . .	37
5.2.2	Control of laser power . . . . .	37
5.2.3	Chopper . . . . .	38
5.2.4	Single mode fiber . . . . .	38
5.2.5	Beam shaper . . . . .	39

5.2.6	Polarizing beam splitter . . . . .	39
5.2.7	Objective lens and pump spot size . . . . .	39
5.2.8	Collecting emitted light . . . . .	40
5.3	White light reflection . . . . .	40
5.4	Position-, momentum-, and energy-resolved measurement . . . . .	41
5.4.1	$x, y$ resolved . . . . .	41
5.4.2	$x, E$ resolved . . . . .	42
5.4.3	$k_x, k_y$ resolved . . . . .	43
5.4.4	$k_x, E$ resolved . . . . .	43
5.5	Coherence measurement ( $x, y$ resolved) . . . . .	44
5.5.1	First arm . . . . .	45
5.5.2	Second arm . . . . .	45
5.5.3	Interference signal at the CCD camera . . . . .	46
5.6	Data evaluation . . . . .	46
<b>6</b>	<b>Previous work by other researchers</b>	<b>49</b>
<b>7</b>	<b>Measured coherence</b>	<b>51</b>
7.1	Condensation threshold and blue-shift of exciton-polariton energy . .	52
7.2	Coherence . . . . .	53
7.2.1	Short distances (Region I) . . . . .	53
7.2.2	Intermediate distances (Region II) . . . . .	55
7.2.3	Very long distances (Region III) . . . . .	55
7.3	Pump-power dependence of the exponent $a_p$ . . . . .	55
7.4	Comparing observed exponent to predicted values . . . . .	58
7.4.1	Determination of the superfluid density $n_s$ . . . . .	58
7.4.2	Determination of the thermal de Broglie wavelength $\lambda_T$ . . . . .	58
7.4.3	Match between predicted and observed exponents . . . . .	60

7.5	Summary of exponent $a_p$ measurements . . . . .	61
<b>8</b>	<b>Condensate fragmentation</b>	<b>63</b>
8.1	Top-hat pump profile . . . . .	63
8.2	Multi-mode condensation . . . . .	64
8.3	Correlation-function . . . . .	65
8.4	Simulated data for top-hat . . . . .	67
8.5	Measured data . . . . .	69
8.6	Recovery of long range order . . . . .	71
8.7	Conclusion about fragmented condensates . . . . .	74
<b>9</b>	<b>Summary and outlook</b>	<b>75</b>
<b>A</b>	<b>Visibility and <math>g^{(1)}</math></b>	<b>77</b>
<b>B</b>	<b>Simulated fast visibility decay</b>	<b>81</b>
<b>C</b>	<b>Simulated power-law</b>	<b>83</b>
<b>D</b>	<b>Transition from power-law to faster decay</b>	<b>85</b>
<b>E</b>	<b>Measured visibilities at different conditions</b>	<b>87</b>
	<b>Bibliography</b>	<b>91</b>

# List of Tables

1.1	Influence of in-plane momentum on exciton-polariton energy and on the Hopfield coefficients. (Calculated data) . . . . .	7
2.1	Landau's criterion . . . . .	12
3.1	Decay mechanisms of the coherence in a two-dimensional superfluid. .	22
4.1	Position (or detuning) dependence of the energy levels and effective masses. . . . .	34



# List of Figures

1.1	Exciton-polariton as the superposition of a cavity photon with an exciton.	5
1.2	Detuning dependence of the energy of the quantum well exciton ( $E_{exc}$ ), the cavity photon ( $E_{cav}$ ), the upper polariton ( $E_{UP}$ ) and the lower polariton ( $E_{LP}$ ).	6
1.3	Calculated effective exciton-polariton mass in dependence of the Hopfield coefficient.	8
2.1	Rigid object and superfluid.	16
3.1	A vortex in the center of a two-dimensional superfluid	23
3.2	BKT transition between free vortices and bound vortex-antivortex pairs.	27
3.3	Diagram of BKT transition.	28
4.1	Pieces of the sample (glued to the copper sample holder)	29
4.2	Structure of the sample	30
4.3	Momentum and energy resolved measurement of the reflected white light.	32
4.4	Determining the $Q$ -factor.	33
4.5	Determining $m_{LP}$ and $E_{LP,0}$ .	33
5.1	Photo of the experimental setup	35
5.2	Setup of the optical pump for creating exciton-polaritons.	36

5.3	Setup for shining white light onto the sample . . . . .	41
5.4	Setup for position-, momentum-, and energy-resolved measurement (with removable far-field lens) . . . . .	42
5.5	Influence of the far-field lens. . . . .	43
5.6	Michelson interferometer setup to measure the phase and the fringe visibility ( $x, y$ resolved) . . . . .	44
5.7	Measured interferogram . . . . .	45
5.8	Intensity of each pixel behaving like a sine function. . . . .	46
7.1	Pump-power dependent dispersion . . . . .	52
7.2	Blue-shift of exciton-polariton energy. . . . .	53
7.3	Measured phase and visibility . . . . .	54
7.4	Fitting various decay functions to the visibility data. . . . .	56
7.5	Pump-power dependence of exponent $a_p$ and peak intensity. . . . .	57
7.6	Determination of the exciton-polariton temperature. . . . .	59
7.7	Measured exponents $a_p$ as a function of estimated inverse superfluid phase-space-density $1/(n_s \lambda_T^2)$ . . . . .	60
7.8	Visibility at $x = \pm 2 \mu\text{m}$ vs. the inverse phase-space-density $1/(n \lambda_T^2)$ . . . . .	61
8.1	Gaussian and top-hat intensity profile. . . . .	64
8.2	Simulated total density $n_{\text{total}}(x, 0)$ compared to the pump-intensity $I_{\text{pump}}(x, 0)$ . . . . .	67
8.3	Simulated data for top-hat excitation. . . . .	68
8.4	Values of the simulated correlation function as a function of $x$ . . . . .	69
8.5	Momentum $k$ and energy $E$ resolved measurement of the condensate with Gaussian and top-hat excitation. . . . .	70
8.6	Measured data with top-hat excitation at low temperature . . . . .	70
8.7	Measured data with top-hat excitation at high temperature . . . . .	71

8.8	Experimental setup for spectrally resolved interference measurement.	72
8.9	Spectrometric resolved interference data. . . . .	73
A.1	Pump-power dependent density distribution. . . . .	78
B.1	Simulated visibility. . . . .	81
C.1	Simulated power-law. . . . .	84
D.1	Transition from power law to fast decay of visibility. . . . .	86
E.1	Measured visibility at a detuning of -1 meV. . . . .	88
E.2	Measured visibility at a detuning of 4 meV. . . . .	89



# Chapter 1

## Exciton-polaritons

For our measurements, we use an exciton-polariton condensate, for which it is possible to study the coherence properties for varying superfluid densities not only near the critical value but also far above that. Exciton-polaritons are 2D bosonic quasiparticles which can be described as the superposition of cavity photons and quantum well excitons [1, 2]. At low temperatures, they exhibit dynamical condensation [3–5]. This condensate of exciton-polaritons can show a vortex-antivortex bound pair [5] as well as single vortices pinned at a defect [6–9]. Exciton-polaritons decay if a photon leaks out of the sample; in this case the leaking photons preserve [4, 10, 11] the energy, in-plane momentum and coherence properties of the polaritons. Michelson interference allows us the measurement of  $g^{(1)}$  of the leaking photons from the exciton-polariton condensate, which makes an exciton-polariton condensate a suitable system for studying the coherence of two-dimensional condensates [12–14].

### 1.1 Micro-cavity photons

A micro-cavity can be formed by two highly reflecting mirrors. In this case, photons can be repeatedly reflected back and forth between the two mirrors and thereby they

are trapped in the cavity between the mirrors. The resonance energy of these trapped photons is determined by the optical width of the cavity.

## 1.2 Quantum well excitons

A quantum well can be formed as a thin layer of a semiconductor material, whose thickness is so small that charge carriers in it are essentially confined to a two-dimensional plain. If a photon is absorbed by the semiconductor material, it can excite an electron from the valence band into the conduction band. Afterwards the electron can move around within the semiconductor, and the missing charge at its former position in the valence band can be described as a positive hole. Due to their different charge, the electron and hole attract each other and tend to bind together. Such a bound electron-hole pair is called an exciton. Since both the electron and the hole are confined to the thin semiconductor layer acting as a quantum well, also the exciton-polariton can be described as a particle in a two-dimensional quantum well.

## 1.3 Coupling between photons and excitons

If such a quantum well is inserted into the micro-cavity, a cavity photon can be absorbed whereby a quantum well exciton is created. This exciton can decay by the re-combination of the electron with the hole, which means that the electron falls back to its previous position in the valence band. During the decay of an exciton, a photon is emitted. This emitted photon is again trapped in the cavity and can later be re-absorbed by the quantum well. If the repeated absorption and emission of photons happens fast enough, the excitation can better be described as not being either an exciton or a photon, but in a quantum mechanical superposition called the

exciton-polariton. The system can be described by the Hamiltonian <sup>1</sup>

$$\hat{H} = \underbrace{E_{\text{cav}} \hat{a}^\dagger \hat{a}}_{=\hat{H}_{\text{cav}}} + \underbrace{E_{\text{exc}} \hat{b}^\dagger \hat{b}}_{=\hat{H}_{\text{exc}}} + \underbrace{g_0 (\hat{a}^\dagger \hat{b} + \hat{b}^\dagger \hat{a})}_{=\hat{H}_{\text{interaction}}}, \quad (1.1)$$

where  $\hat{a}^\dagger$  is the creation and  $\hat{a}$  the annihilation operator for a photon, so that  $\hat{H}_{\text{cav}}$  is simply the energy per photon  $E_{\text{cav}}$  multiplied with the counting operator  $\hat{a}^\dagger \hat{a}$  for the photons. In the same way,  $\hat{b}$  is the annihilation operator for an exciton and  $E_{\text{exc}}$  the energy per exciton. The interaction between cavity photons and quantum well excitons is proportional to the interaction strength  $g_0$  and described by  $\hat{H}_{\text{interaction}}$ , where  $\hat{a}^\dagger \hat{b}$  represents the decay of an exciton with simultaneous emission of a photon, whereas  $\hat{b}^\dagger \hat{a}$  represents the creation of an exciton through the absorption of a photon. The Hamiltonian of the system can be uncoupled by defining the new annihilation operators as

$$\hat{U} = X\hat{a} - C\hat{b} \quad (1.2)$$

for the upper polariton and

$$\hat{L} = C\hat{a} + X\hat{b} \quad (1.3)$$

for the lower polariton, where the scalars  $C$  and  $X$  are chosen in such a way that

$$|X|^2 = \frac{1}{2} \left( 1 + \frac{\Delta E}{\sqrt{(\Delta E)^2 + (2g_0)^2}} \right) \quad (1.4)$$

and

$$|C|^2 = 1 - |X|^2. \quad (1.5)$$

---

<sup>1</sup>This simplified formula 1.1 considers only photons and excitons without any in-plane momentum. To consider the possibility of different in-plane momenta  $\mathbf{k}$  one has to sum over the possible  $\mathbf{k}$ -modes which gives [15] an equation of the form  $\hat{H} = \sum_{\mathbf{k}} E_{\text{cav},\mathbf{k}} \hat{a}_{\mathbf{k}}^\dagger \hat{a}_{\mathbf{k}} + \sum_{\mathbf{k}} E_{\text{exc},\mathbf{k}} \hat{b}_{\mathbf{k}}^\dagger \hat{b}_{\mathbf{k}} + \sum_{\mathbf{k}} g_0 (\hat{a}_{\mathbf{k}}^\dagger \hat{b}_{\mathbf{k}} + \hat{b}_{\mathbf{k}}^\dagger \hat{a}_{\mathbf{k}})$ .

The quantity

$$\Delta E := E_{\text{cav}} - E_{\text{exc}} \quad (1.6)$$

is known as the detuning which is defined as the difference between the cavity photon resonance energy and the quantum well exciton energy.

With these definitions, the uncoupled Hamiltonian of the system becomes

$$\hat{H} = \underbrace{E_{\text{LP}} \hat{L}^\dagger \hat{L}}_{=\hat{H}_{\text{LP}}} + \underbrace{E_{\text{UP}} \hat{U}^\dagger \hat{U}}_{=\hat{H}_{\text{UP}}} \quad (1.7)$$

and the energies of the upper (UP) and lower (LP) polaritons can be calculated as

$$E_{\text{UP,LP}} = \frac{1}{2} \left( E_{\text{exc}} + E_{\text{cav}} \pm \sqrt{(2g_0)^2 + \Delta E^2} \right). \quad (1.8)$$

This means by describing the system as consisting of upper and lower polaritons, the total energy is simply the lower polariton energy times the number of lower polaritons plus the upper polariton energy times their number; no additional interaction term occurs, which means in matrix notation that the Hamiltonian has been diagonalized [15].

The micro-cavity (figure 1.1) is usually intentionally produced in such a way that its thickness and therefore also its cavity photon resonance energy  $E_{\text{cav}}$  changes with position, whereas the energy  $E_{\text{exc}}$  of the quantum well excitons is assumed to be position-independent. Figure 1.2 shows a typical result for the calculated different energy levels as a function of the detuning, which itself is a function of the position. One sees that for negative detuning, which is also known as the “red detuned” region, the lower polariton becomes increasingly similar to the cavity photon, whereas for positive (or “blue”) detuning, it becomes exciton-like. The upper polariton behaves exactly the opposite way. At zero detuning, this means at the point where the cavity photon has exactly the same energy as the quantum well exciton, the energy

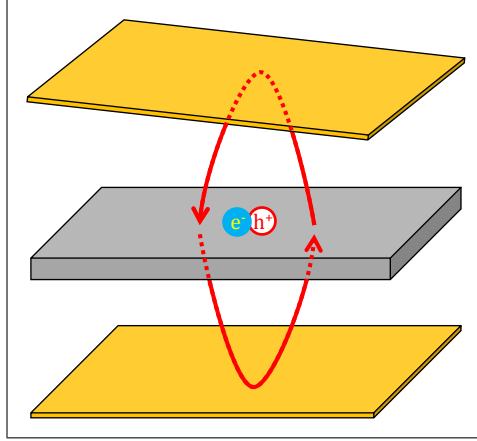


Figure 1.1: Exciton-polariton as the superposition of a cavity photon with an exciton. The thickness of the cavity (and therefore also the detuning) is position dependent.

difference between the upper and lower polaritons is the Rabi splitting of  $2g_0$ . For the condensate measurements, we only use lower polaritons, since these are the particles with the lower energy which are created if we excite the system, Therefore in the following, “exciton-polaritons” usually refers only to the lower polaritons.

### 1.3.1 Photon and exciton fraction

The scalars  $|X|^2$  and  $|C|^2$  from equations 1.4 and 1.5 are known as the Hopfield coefficients [15,16]. The excitonic fraction of the lower polariton is  $|X|^2$  whereas  $|C|^2$  is its photonic fraction. This means at zero detuning where  $|X|^2 = |C|^2 = \frac{1}{2}$ , the exciton-polaritons have exactly half exciton and half photon properties. In the red detuned ( $\Delta E < 0$ ) region, the lower polariton is photon-like ( $|X|^2 < |C|^2$ ) and in the far red detuned area ( $\Delta E \ll -g_0$ ), the lower polariton is nearly the same as a photon ( $|X|^2 \approx 0$ ;  $|C|^2 \approx 1$ ). In the blue detuned area ( $\Delta E > 0$ ) the opposite is true and the lower polariton becomes more exciton-like ( $|X|^2 > |C|^2$ ).

The upper polariton behaves in the opposite way (equation 1.2), meaning it is exciton-like for red detuning ( $\Delta E < 0$ ;  $|X|^2 < |C|^2$ ) and photon-like for blue detuning

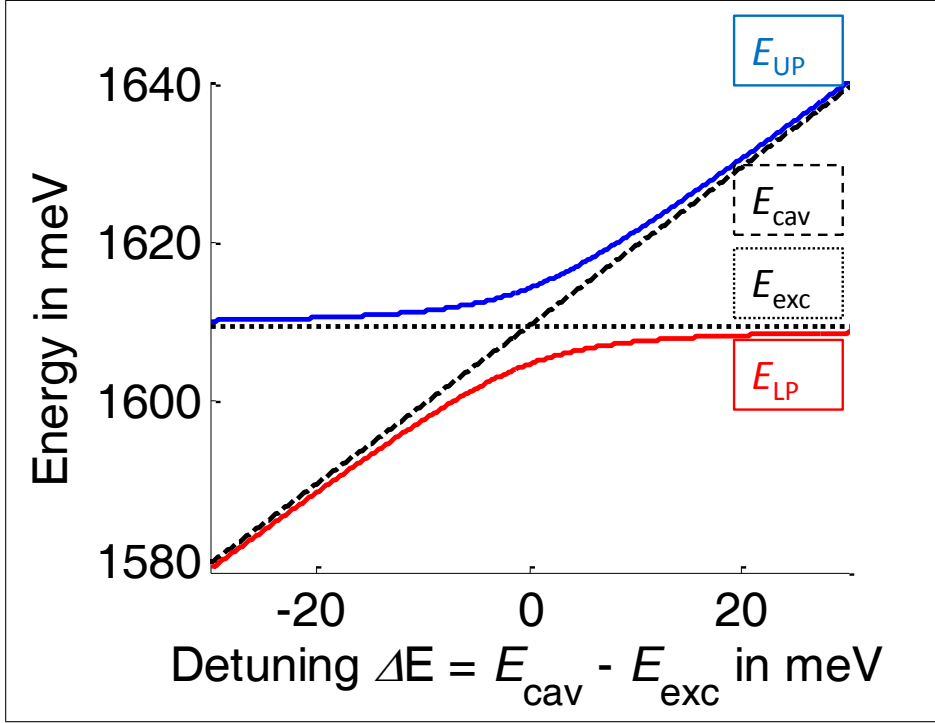


Figure 1.2: Detuning dependence of the energy of the quantum well exciton ( $E_{\text{exc}}$ ), the cavity photon ( $E_{\text{cav}}$ ), the upper polariton ( $E_{\text{UP}}$ ) and the lower polariton ( $E_{\text{LP}}$ ). Avoided crossing is clearly visible. The cavity is usually produced in such a way that the detuning steadily changes with position, which means that the horizontal axis could also be understood as the position.

$$(\Delta E > 0; |X|^2 > |C|^2).$$

### 1.3.2 Momentum dependence of the Hopfield coefficients

Since the excitons are confined into the two-dimensional quantum well and the photons are confined into the two-dimensional cavity, the exciton-polaritons can also move within the two-dimensional plane. By doing this, they have an in-plane momentum  $\mathbf{k} = (k_x; k_y)$ , and the momentum conservation implies that such a moving exciton-polariton must be the superposition of an exciton and photon which both also have this same momentum  $\mathbf{k}$ . This gives an additional contribution to their energies

as

$$E_{\text{cav}}(\mathbf{k}) = E_{\text{cav},0} + \frac{\hbar^2 \mathbf{k}^2}{2m_{\text{cav}}} \quad (1.9)$$

and

$$E_{\text{exc}}(\mathbf{k}) = E_{\text{exc},0} + \frac{\hbar^2 \mathbf{k}^2}{2m_{\text{exc}}}. \quad (1.10)$$

The additional kinetic energy of the exciton can be neglected since the effective mass  $m_{\text{exc}}$  is much larger than the effective cavity photon mass  $m_{\text{cav}}$ . This also means that the momentum  $\mathbf{k}$  affects the detuning

$$\Delta E(\mathbf{k}) = -E_{\text{exc}}(\mathbf{k}) + E_{\text{cav}}(\mathbf{k}) \approx \underbrace{-E_{\text{exc},0} + E_{\text{cav},0}}_{:=\Delta E_0} + \frac{\hbar^2 \mathbf{k}^2}{2m_{\text{cav}}} = \Delta E_0 + \frac{\hbar^2 \mathbf{k}^2}{2m_{\text{cav}}}, \quad (1.11)$$

which also affects the Hopfield coefficients  $|X|^2$  and  $|C|^2$  and other properties like exciton-polariton mass and lifetime which depend on the Hopfield coefficients.

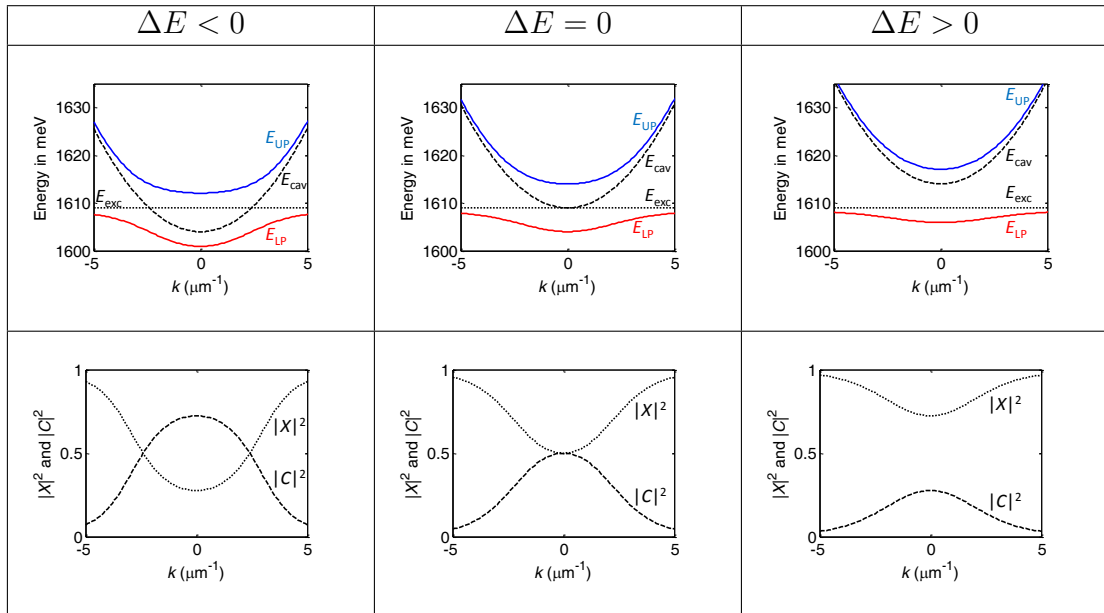


Table 1.1: Influence of in-plane momentum on exciton-polariton energy and on the Hopfield coefficients. (Calculated data)

### 1.3.3 Effective mass of exciton-polaritons

From

$$\underbrace{\frac{\hbar^2 \mathbf{k}^2}{2m_{\text{LP}}}}_{=E_{\text{LP,kinetic}}} = |X|^2 \underbrace{\frac{\hbar^2 \mathbf{k}^2}{2m_{\text{exc}}}}_{=E_{\text{exc,kinetic}}} + |C|^2 \underbrace{\frac{\hbar^2 \mathbf{k}^2}{2m_{\text{cav}}}}_{=E_{\text{cav,kinetic}}}, \quad (1.12)$$

it follows that the effective mass  $m_{\text{LP}}$  of the lower polariton is determined by

$$m_{\text{LP}} = \left( \frac{|X|^2}{m_{\text{exc}}} + \frac{|C|^2}{m_{\text{cav}}} \right)^{-1} \approx \frac{m_{\text{cav}}}{|C|^2}, \quad (1.13)$$

where the contribution of  $\frac{1}{m_{\text{exc}}}$  can be neglected (for  $|X|^2 \gg |C|^2$ ) because  $\frac{1}{m_{\text{exc}}} \ll \frac{1}{m_{\text{cav}}}$  [17]. This implies that near zero detuning the effective mass  $m_{\text{LP}}$  of the exciton-polariton is approximately twice the effective mass  $m_{\text{cav}}$  of the cavity photon.

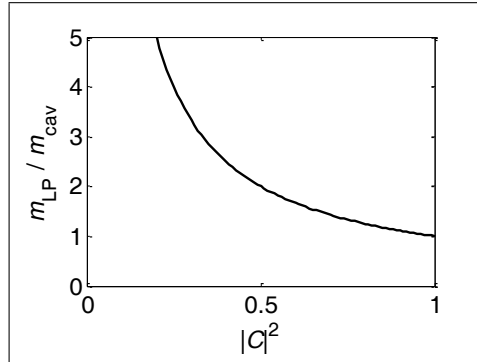


Figure 1.3: Calculated effective exciton-polariton mass in dependence of the Hopfield coefficient.

### 1.3.4 Lifetime of exciton-polaritons

The cavity photons by themselves (assuming no interaction with excitons) have some lifetime  $t_{\text{cav}}$ , which corresponds to a decay rate of  $t_{\text{cav}}^{-1}$ . They primarily decay by leaking out of the cavity through the mirrors, and therefore  $t_{\text{cav}}$  is primarily determined by the quality of the mirrors. Experimentally,  $t_{\text{cav}}$  can be measured in the far red

detuned area of the sample where the cavity photon energy is too low to excite excitons, so that any interaction between photons and exciton-states in the quantum well is negligible.

Excitons in the quantum well have a total decay rate of

$$t_{\text{exc,total}}^{-1} = t_{\text{exc,radiative}}^{-1} + t_{\text{exc,non-radiative}}^{-1}, \quad (1.14)$$

which has contributions both from radiative and non-radiative decay.

The decay rate of exciton-polaritons is therefore determined by

$$t_{\text{LP}}^{-1} = |X|^2 t_{\text{exc,non-radiative}}^{-1} + |C|^2 t_{\text{cav}}^{-1}, \quad (1.15)$$

which considers that an exciton-polariton can decay through photon leakage (while being in the photon-state for which the probability is  $|C|^2$ ) or through non-radiative exciton decay (while being in the exciton-state for which the probability is  $|X|^2$ ). Here, only the non-radiative exciton-decay contributes to the decay rate of the exciton-polariton, since the radiative exciton decay only contributes to the repeated transformation between exciton and photon instead of causing a decay of the exciton-polariton.

Usually the non-radiative exciton decay rate is negligible ( $t_{\text{exc,non-radiative}}^{-1} \ll t_{\text{cav}}^{-1}$ ), which simplifies [18] equation 1.15 to

$$t_{\text{LP}} = \frac{t_{\text{cav}}}{|C|^2}. \quad (1.16)$$

### 1.3.5 Spin

Exciton-polaritons are the superposition of a photon (with spin 1) and a heavy hole Wannier-Mott exciton [15]. The exciton itself consists of an electron (with spin  $\frac{1}{2}$ )

and a heavy hole (with spin  $\frac{3}{2}$ ), which means that the exciton polariton spin can be 1 or 2. The excitons with spin 2 are known as dark excitons because they cannot be excited by light (with spin 1) due to spin conservation. On the other hand side, the excitons with spin 1 can interact with light, and they form the exciton-polaritons. These exciton-polaritons also have an effective spin of  $\pm 1$ , which means that they show bosonic behavior.

### 1.3.6 Condensation of exciton-polaritons

#### Condensation temperature

As shown in equation 1.13, the effective mass of exciton-polaritons is similar to the mass of cavity photons. Therefore exciton-polaritons have a very low mass, which is approximately  $10^{-10}$  times the mass of a typical atom. As a result of this, exciton-polaritons can form a condensate [3, 4, 15] at a temperature of several kelvin <sup>2</sup> which is much easier to reach than the  $\approx 100$  nK [23] which are needed for atomic Bose-Einstein condensation.

#### Stimulated scattering

The condensation of exciton-polaritons is facilitated by stimulated scattering [24–29]; this means the rate at which they condense into the ground state is proportional to  $(N_0 + 1)$  where  $N_0$  is the current population of the ground state.

---

<sup>2</sup>Most of the measurements described in this thesis have been done at liquid helium temperature of  $\approx 5$  K. With other materials [19] like large band gap semiconductors [20, 21] or polymer crystals [22] exciton polariton condensation is possible even at room temperature.

# Chapter 2

## Superfluidity

Condensation of bosonic particles like exciton-polaritons is accompanied both by superfluid behavior and by the build-up of spatial coherence over long distances.

### 2.1 Landau's criterion

The existence of superfluidity can be explained using Landau's criterion [30–33]. If a normal fluid flows over a surface, its flow is slowed down through scattering processes occurring between the fluid and the surface. Landau's criterion shows that under certain conditions these scattering processes cannot happen because after scattering, the overall energy of the system would be higher than before. If these conditions are fulfilled, the fluid can flow over the surface without scattering, which means that it exhibits superfluid behaviour. To understand Landau's criterion, one can imagine a fluid which flows with velocity  $\mathbf{v}$  over a surface.

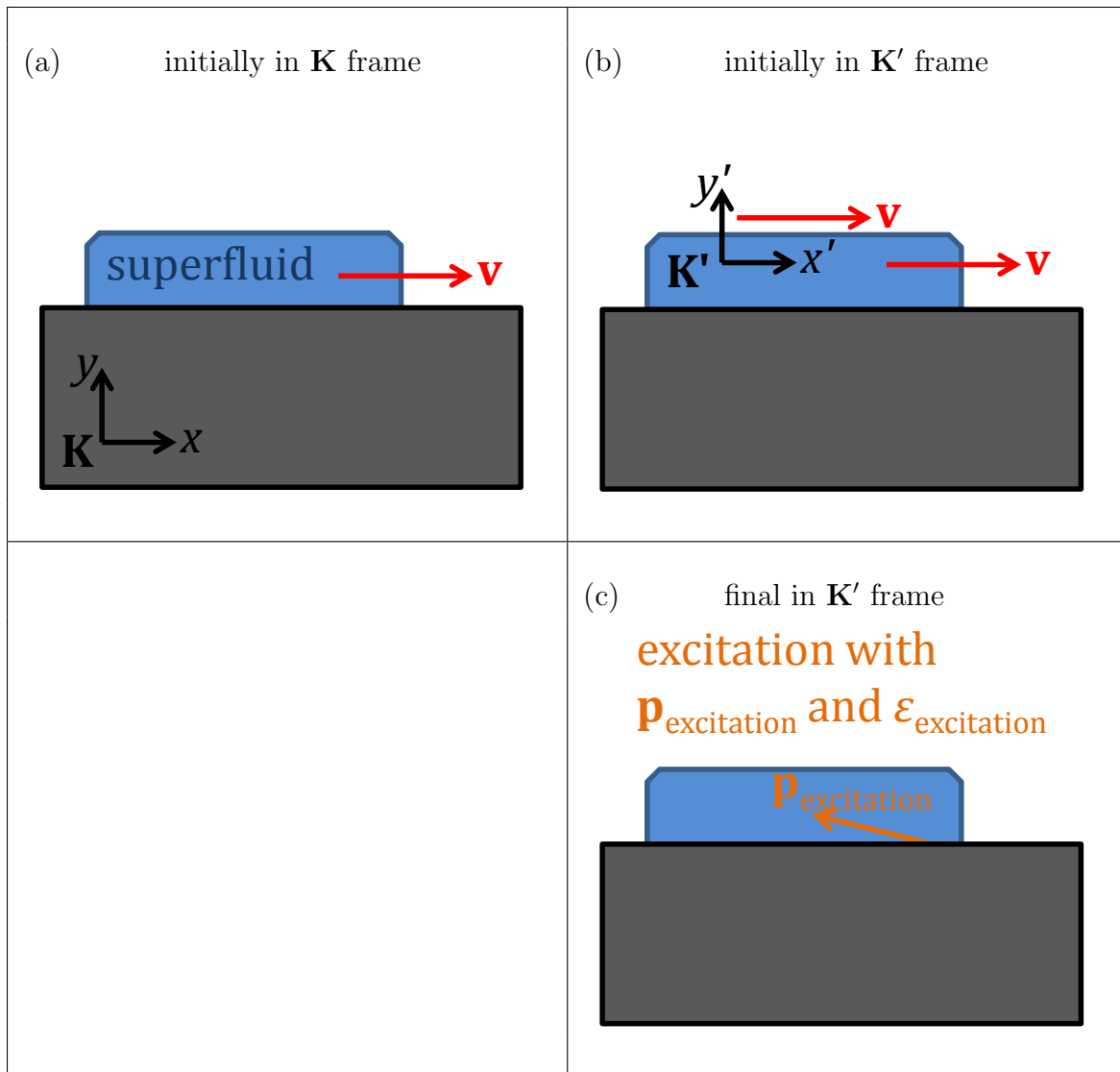


Table 2.1: Landau's criterion

### 2.1.1 Initially in $\mathbf{K}$ frame

In the inertial frame of reference  $\mathbf{K}$  in which the surface (but not the superfluid) is at rest (table 2.1 (a)), the initial energy of the superfluid is

$$E_{\text{initial}} = \underbrace{E_0}_{=E_{\text{internal, initial}}} + \underbrace{\frac{M_{\text{fluid}} |\mathbf{v}|^2}{2}}_{=E_{\text{kinetic, initial}}}, \quad (2.1)$$

where  $E_0$  is the internal energy of the fluid and  $M_{\text{fluid}}$  is its mass.

The momentum of the fluid is

$$\mathbf{P}_{\text{initial}} = M_{\text{fluid}} \mathbf{v} \quad (2.2)$$

in the same system.

### 2.1.2 Initially in $\mathbf{K}'$ frame

If one describes (table 2.1 (b)) the fluid in the inertial frame of reference  $\mathbf{K}'$  which moves with velocity  $\mathbf{v}$  relative to the frame  $\mathbf{K}$ , then the fluid is initially at rest (in  $\mathbf{K}'$ ) and its energy is

$$E'_{\text{initial}} = \underbrace{E_0}_{=E'_{\text{internal, initial}}}, \quad (2.3)$$

since there is no kinetic energy, whereas the internal energy of the fluid is the same in any reference system, and the momentum of the superfluid

$$\mathbf{P}'_{\text{initial}} = 0 \quad (2.4)$$

also disappears in the  $\mathbf{K}'$  frame.

### 2.1.3 Final in $\mathbf{K}'$ frame

If the fluid is slowed down by friction or any other interaction with the surface, this can be described through some excitation of the fluid. If this excitation corresponds to an energy  $\epsilon_{\text{excitation}}$  and momentum  $\mathbf{p}_{\text{excitation}}$ , then after the creation of the excitation, the superfluid has an final energy

$$E'_{\text{final}} = E_0 + \epsilon_{\text{excitation}} \quad (2.5)$$

and momentum

$$\mathbf{P}'_{\text{final}} = \mathbf{p}_{\text{excitation}} \quad (2.6)$$

in the  $\mathbf{K}'$  frame (table 2.1 (c)).

### 2.1.4 Final in $\mathbf{K}$ frame

Now, if one describes the final system in the  $\mathbf{K}$  frame, the fluid has a momentum of

$$\mathbf{P}_{\text{final}} = \mathbf{P}'_{\text{final}} + M_{\text{fluid}}\mathbf{v} = \mathbf{p}_{\text{excitation}} + M_{\text{fluid}}\mathbf{v} \quad (2.7)$$

and a final energy of

$$\begin{aligned} E_{\text{final}} &= E_{\text{internal, final}} + E_{\text{kinetic, final}} = \\ &= E_{\text{internal, final}} + \frac{|\mathbf{P}_{\text{final}}|^2}{2M_{\text{fluid}}} = \\ &= E_{\text{internal, final}} + \frac{|\mathbf{p}_{\text{excitation}} + M_{\text{fluid}}\mathbf{v}|^2}{2M_{\text{fluid}}} = \\ &= \underbrace{E_{\text{internal, final}}}_{E'_{\text{internal, final}}} + \underbrace{\frac{|\mathbf{p}_{\text{excitation}}|^2}{2M_{\text{fluid}}}}_{E'_{\text{kin, final}}} + \frac{M_{\text{fluid}}|\mathbf{v}|^2}{2} + \frac{\mathbf{p}_{\text{excitation}}\mathbf{v}}{M_{\text{fluid}}} = \\ &\quad \underbrace{\hspace{10em}}_{=E'_{\text{final}}=E_0+\epsilon_{\text{excitation}}} \end{aligned}$$

$$= \underbrace{E_0 + \frac{M_{\text{fluid}} |\mathbf{v}|^2}{2}}_{E_{\text{initial}}} + \underbrace{\epsilon_{\text{excitation}} + \frac{\mathbf{p}_{\text{excitation}} \mathbf{v}}{M_{\text{fluid}}}}_{=:\Delta E}. \quad (2.8)$$

### 2.1.5 Energy change

So one sees (in the  $\mathbf{K}$  frame) that the scattering process causes a change of the energy by

$$\Delta E = \epsilon_{\text{excitation}} + \frac{\mathbf{p}_{\text{excitation}} \mathbf{v}}{M_{\text{fluid}}}. \quad (2.9)$$

The scattering can only happen if it causes a decrease of the energy, this means  $\Delta E < 0$ , and from equation 2.9 one sees that this is only possible if  $|\mathbf{v}| > \frac{\epsilon_{\text{excitation}}}{|\mathbf{p}_{\text{excitation}}|}$  and at the same time  $\mathbf{p}_{\text{excitation}} \mathbf{v} < 0$ . This means for

$$|\mathbf{v}| < \underbrace{\min \left( \frac{\epsilon_{\text{excitation}} (\mathbf{p}_{\text{excitation}})}{|\mathbf{p}_{\text{excitation}}|} \right)}_{=:\mathbf{v}_{\text{threshold}}}, \quad (2.10)$$

no excitations can be created and superfluid flow occurs, whereas normal fluid flow occurs for velocities above this threshold.

If the excitation corresponds to the usual parabolic dispersion relation

$$\epsilon_{\text{excitation}}^{(\text{parabolic})} = \frac{|\mathbf{p}_{\text{excitation}}|^2}{2m_{\text{excitation}}}, \quad (2.11)$$

then  $\mathbf{v}_{\text{threshold}} = 0$ , which means that scattering is possible at any flow velocity  $\mathbf{v}$ , and therefore no superfluidity exists.

However under certain conditions the excitations can have a non-parabolic dispersion relation. For example excitations in an exciton-polariton condensate show a Bogoliubov dispersion [11, 34] of the form

$$\epsilon_{\text{excitation}} = \sqrt{\alpha^2 |\mathbf{p}_{\text{excitation}}|^2 + \beta^4 |\mathbf{p}_{\text{excitation}}|^4} \quad (2.12)$$

where  $\alpha$  and  $\beta$  are system dependent constants. For small momentum ( $|\mathbf{p}_{\text{excitation}}| \approx 0$ ), the Bogoliubov dispersion can be approximated as

$$\epsilon_{\text{excitation}} \approx \alpha |\mathbf{p}_{\text{excitation}}|, \quad (2.13)$$

and with equation 2.10, this means that the fluid (in this case an exciton-polariton condensate) shows superfluid behaviour as long as it flows with a velocity of less than  $\mathbf{v}_{\text{threshold}} = \alpha$ .

## 2.2 Vortices

Another famous property of a superfluid is the existence of quantized vortices.

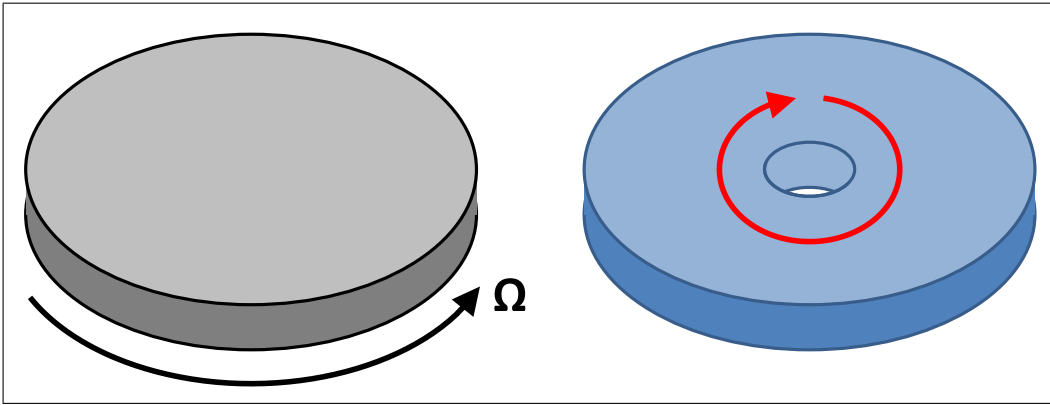


Figure 2.1: Rigid object (left) and superfluid (right).

### 2.2.1 Rotating a rigid object

If a rigid object (figure 2.1) rotates with an angular frequency of  $|\boldsymbol{\Omega}|$ , the velocity of each point in the object is

$$\mathbf{v} = \boldsymbol{\Omega} \times \mathbf{r} \quad (2.14)$$

where  $\mathbf{r}$  is the vector from the rotation axis to the respective point. This means (for  $|\boldsymbol{\Omega}| \neq 0$ ) the curl

$$\nabla \times \mathbf{v} = \nabla \times (\boldsymbol{\Omega} \times \mathbf{r}) = 2\boldsymbol{\Omega} \quad (2.15)$$

must be different from zero.

### 2.2.2 Impossibility to rotate a superfluid

A superfluid can be described by the wave-function

$$\Psi(\mathbf{r}, t) = \sqrt{n_s(\mathbf{r}, t)} e^{i\Theta(\mathbf{r}, t)}, \quad (2.16)$$

where  $n_s$  is the local superfluid density and  $\Theta$  its phase. This gives the local velocity of

$$\mathbf{v}(\mathbf{r}, t) = \frac{\mathbf{p}(\mathbf{r}, t)}{m} = \frac{\hbar}{m} \nabla \Theta(\mathbf{r}, t) \quad (2.17)$$

and a curl [30] of

$$\nabla \times \mathbf{v}(\mathbf{r}, t) = \nabla \times \left( \frac{\hbar}{m} \nabla \Theta(\mathbf{r}, t) \right) = 0. \quad (2.18)$$

This shows that a superfluid can not rotate as a whole like a rigid object, since this requires a non-zero value of  $\nabla \times \mathbf{v}$  as shown in equation 2.15. Since a superfluid can not rotate as a whole like a rigid object, the only way for it to have a non-zero angular momentum is through the presence of quantized vortices.

A superfluid with a vortex (centered at the origin of the coordinate system) can be described by the wave-function

$$\psi(\mathbf{r}) = \sqrt{n_s(\mathbf{r})} e^{is\phi} \quad (2.19)$$

where  $s = \pm 1$  is an integer <sup>1</sup>,  $\phi$  is the polar coordinate, and the superfluid density

---

<sup>1</sup>In theory, larger values like  $s = 2$  are possible, but such a vortex would immediately split into

is zero <sup>2</sup> at the center of the vortex. Each vortex contributes a certain quantized angular momentum, and a system with a large total angular momentum will contain many vortices. Such vortices have been experimentally realized by stirring an atomic Bose-Einstein condensate [35].

---

two vortices with  $s = 1$  which maintains the total angular momentum but reduces the energy.

<sup>2</sup>For  $n_s(0) \neq 0$ , the phase at  $\mathbf{r} = 0$  can not be defined, and as explained in chapter 3.3.3, the flow velocity would diverge.

# Chapter 3

## Spatial coherence

In addition to superfluidity, a two-dimensional exciton-polariton condensate also exhibits spatial coherence over long distances.

### 3.1 Correlation function

In general, the spatial coherence between point  $\mathbf{r}_1$  at time  $t_1$  and point  $\mathbf{r}_2$  at time  $t_2$  can be quantitatively described by the first-order spatial coherence function

$$g^{(1)}(\mathbf{r}_1, t_1, \mathbf{r}_2, t_2) = \frac{|\langle \hat{\Psi}^\dagger(\mathbf{r}_1, t_1) \hat{\Psi}(\mathbf{r}_2, t_2) \rangle|}{\sqrt{\langle \hat{\Psi}^\dagger(\mathbf{r}_1, t_1) \hat{\Psi}(\mathbf{r}_1, t_1) \rangle} \sqrt{\langle \hat{\Psi}^\dagger(\mathbf{r}_2, t_2) \hat{\Psi}(\mathbf{r}_2, t_2) \rangle}} \quad (3.1)$$

which has been normalized in such a way that it reaches the value of 1 for perfect coherence and 0 for no coherence [13, 14]. By considering only the spatial coherence in the case  $t_1 = t_2$  and approximating the destruction operator  $\hat{\Psi}$  by the wavefunction

$\Psi$ , the spatial coherence function can be written as

$$g^{(1)}(\mathbf{r}_1, \mathbf{r}_2) = \frac{|\langle \Psi^*(\mathbf{r}_1) \Psi(\mathbf{r}_2) \rangle|}{\sqrt{\langle |\Psi(\mathbf{r}_1)|^2 \rangle} \sqrt{\langle |\Psi(\mathbf{r}_2)|^2 \rangle}}, \quad (3.2)$$

where the wavefunction  $\Psi$  is normalized in such a way that  $n(\mathbf{r}) = |\Psi(\mathbf{r})|^2$  is the exciton-polariton density at point  $\mathbf{r}$  and  $|\Psi(\mathbf{r})|^2$  has the units of  $\mu\text{m}^{-2}$  or exciton-polaritons per  $\mu\text{m}^2$ .

## 3.2 Coherence of three dimensional condensates

In the case of three-dimensional condensates, like an atomic Bose-Einstein condensate, the first order spatial coherence function over large distances is equal to the condensation fraction

$$\lim_{|\mathbf{r}_1 - \mathbf{r}_2| \rightarrow \infty} g^{(1)}(\mathbf{r}_1, \mathbf{r}_2) = \frac{N_0}{N} \quad (3.3)$$

where the condensation fraction  $\frac{N_0}{N}$  is the ratio between the number  $N_0$  of condensed atoms and the total atom number  $N$  [36].

## 3.3 Coherence of two dimensional systems

In the case of two-dimensional (2D) systems, coherence can be reduced by several decay mechanisms, which include the thermal excitation of phononic long wavelength phase fluctuations as well as vortices.

### 3.3.1 Lack of real long-range order

It has been theoretically shown that true long range order cannot exist in infinite uniform two-dimensional systems at non-zero temperature. This is known as the

Hohenberg-Mermin-Wagner theorem [37, 38]. The reason is that at any non-zero temperatures, thermally excited fluctuations will eventually destroy the coherence over long distances.

### 3.3.2 Possibility of quasi-long-range order

From the Hohenberg-Mermin-Wagner theorem one only knows that in a two-dimensional system the coherence over infinite distances will be zero. However in interacting systems, superfluidity can persist at non-zero temperature. In this case, the spatial decay of the coherence can be extremely slow. Since all experimentally relevant systems have only a finite size, it is possible that the coherence decays so slow that a high level of coherence exists throughout the entire system. This is known as quasi-long-range order [39], and can be understood with the Berezinskii-Kosterlitz-Thouless (BKT) [40, 41] theory.

### 3.3.3 Decay mechanisms for spatial coherence

There are several mechanisms (table 3.1) by which the spatial coherence of a two-dimensional superfluid can be destroyed. The most important are vortices (which can occur either as free vortices or as a bound vortex-antivortex pair) and thermally excited phononic phase fluctuations [42, 43].

#### Free vortices

Vortices are characterized by a vanishing superfluid density in their cores and a phase change of  $2\pi$  (or  $-2\pi$  in the case of an antivortex) around them. Free vortices, meaning those which are neither bound in pairs nor trapped at a specific location, can move throughout the sample. Since they affect the phase of the entire condensate, the phase relation between largely separated points becomes arbitrary and the phase

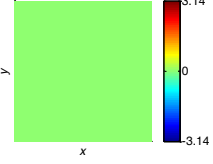
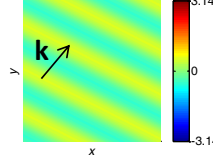
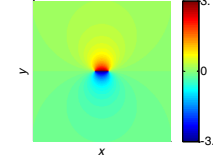
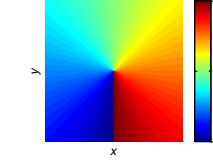
$T \equiv 0$	$T > 0$		$T \gg 0$
(theoretically)	(low temperature)		(high temperature)
	phononic phase-fluctuations	vortices	
		vortex-antivortex-pairs	free vortices
			
	causes slow decay of coherence	does not affect coherence over long distances	destroys coherence over long distances
Perfect phase coherence	Quasi long range order		No coherence over long distances

Table 3.1: Decay mechanisms of the coherence in a two-dimensional superfluid. The images show the simulated phase of a condensate under the respective conditions. They show that phononic excitations weakly affect the phase throughout the system; bound vortex-antivortex-pairs only affect the local phase in their vicinity; a free vortex strongly affects the phase throughout the entire system.

coherence is destroyed. This means in the presence of free vortices, no long range order can exist and the spatial correlation function over medium to long distances is zero. Free vortices will be excited if they result in a negative contribution to the free energy  $F = E - TS$  of the system, where  $E$  is the energy,  $S$  the entropy and  $T$  the temperature [42].

The energy  $E$  of a free vortex can be calculated through its kinetic energy with respect to the superfluid flow. For this, one can assume that the vortex (or antivortex) with a core-radius  $\xi$  is in the center of a superfluid with radius  $R$  (figure 3.1). In this case, the wavefunction can be described as  $\psi(\mathbf{r}) = \sqrt{n_s(r)}e^{\pm i\phi}$  where  $n_s$  is the superfluid density (with units  $\mu\text{m}^{-2}$ ), and the polar coordinates  $(r, \phi)$  are expressed

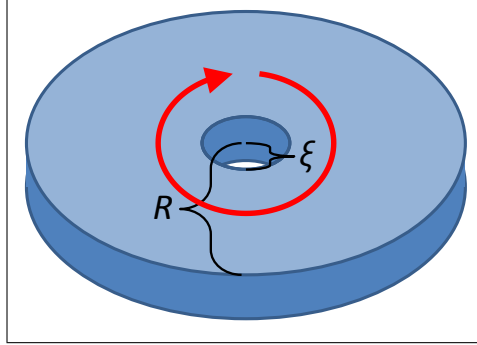


Figure 3.1: A vortex in the center of a two-dimensional superfluid

relative to the pole which coincides with the center of both the vortex and the condensate. The phase factor  $e^{\pm i\phi}$  means that the phase changes by  $\pm 2\pi$  if one walks around the vortex core, and this sign of the phase change can be positive or negative depending on whether we have a vortex or an antivortex. With  $\Theta(\mathbf{r})$  being the phase of the wave function  $\psi(\mathbf{r})$ , the local velocity of the superfluid flow around the vortex is

$$v(\mathbf{r}) = \left| \frac{\hbar}{m_{\text{eff}}} \nabla \Theta(\mathbf{r}) \right| = \left| \pm \frac{\hbar}{m_{\text{eff}}} \nabla \phi \right| = \frac{\hbar}{m_{\text{eff}} r}. \quad (3.4)$$

This implies that there can be no superfluid at the center of the vortex, since its flow velocity would be infinite. If one assumes that the superfluid density vanishes within the vortex core, then  $n_s(\mathbf{r})$  is equal to some constant value  $n_s$  for  $\xi < r < R$  and  $n_s(\mathbf{r}) = 0$  outside of this range.

The energy of the vortex can be calculated by integrating the local kinetic energy of the superfluid flow as

$$\begin{aligned} E &= \int \frac{m_{\text{eff}} n_s(\mathbf{r})}{2} (v(\mathbf{r}))^2 d^2 \mathbf{r} = \\ &= \int_{\xi}^R \frac{m_{\text{eff}} n_s}{2} \left( \frac{\hbar}{m_{\text{eff}} r} \right)^2 2\pi r dr = \\ &= \frac{\hbar^2 \pi n_s}{m_{\text{eff}}} \ln \left( \frac{R}{\xi} \right) = \end{aligned}$$

$$= n_s \lambda_T \frac{k_B T}{2} \ln \left( \frac{R}{\xi} \right), \quad (3.5)$$

where

$$\lambda_T = \frac{h}{\sqrt{2\pi m_{\text{eff}} k_B T}} \quad (3.6)$$

is the thermal de Broglie wavelength. The entropy  $S$  of a vortex is proportional to the logarithm of the number of positions where the vortex can be; it can be calculated as

$$S = k_B \ln \left( \frac{\pi R^2}{\pi \xi^2} \right) = 2k_B \ln \left( \frac{R}{\xi} \right), \quad (3.7)$$

where  $\pi R^2$  is the system size and  $\pi \xi^2$  is the size of the vortex core. This gives the free energy  $F$  of the vortex as

$$F = E - TS = \left( n_s \lambda_T^2 - 4 \right) \underbrace{\frac{k_B T}{2} \ln \left( \frac{R}{\xi} \right)}_{\text{always} > 0} \quad (3.8)$$

which is negative precisely if  $n_s \lambda_T^2 < 4$ . This means if  $n_s \lambda_T^2$  drops below 4, free vortices will be excited and they will destroy any long-range spatial coherence. However for  $n_s \lambda_T^2 > 4$ , this means at high superfluid densities and low temperatures, there will be no free vortices and therefore spatial coherence over large distances is possible [42].

### Bound vortex-antivortex pairs

Vortices can also exist in bound vortex-antivortex-pairs [44, 45]. The only difference between a vortex and an antivortex is that the phase on a path around its core changes by  $+2\pi$  in the case of a vortex, and by  $-2\pi$  in the case of an antivortex. In such a pair each vortex is always in close spatial proximity to its corresponding antivortex, and at large distances from the pair, the influence on the phase of the vortex is canceled out by the antivortex [42, 43]. For example on a path around this pair, the phase

is zero. This means vortex-antivortex pairs do not affect the spatial coherence over long distances. As shown previously, in a condensate with  $n_s \lambda_T^2 > 4$ , there are no free vortices. However if this condensate is large enough, one can argue that it must always contain bound vortex-antivortex-pairs. The energy  $E_{\text{pair}}$  of such a bound pair is just some small constant value; it is independent of the size of the condensate since the bound pair only locally affects the wave function of the condensate in its close proximity. However the entropy which a large superfluid gains through the presence of a bound pair is similar <sup>1</sup> to the entropy of a free vortex, this means it is approximately proportional to the logarithm of the system size. Therefore in the limes of large superfluids with  $R \rightarrow \infty$ , the free energy  $F_{\text{pair}} = E_{\text{pair}} - TS_{\text{pair}}$  behaves like  $-\ln(R)$  and approaches  $-\infty$ . This means in a sufficiently large condensate even with  $n_s \lambda_T^2 > 4$  and without free vortices, there will always be bound vortex-antivortex-pairs. In such a condensate, spatial coherence can exist over large distances, since the influence of each vortex is cancelled out by its bound antivortex. A superfluid which contains only bound vortex-antivortex-pairs is often called to be in the Berezinskii-Kosterlitz-Thouless (BKT) state.

### 3.3.4 Phononic phase fluctuations

In the BKT state where the influence of each vortex is cancelled out by its bound antivortex, the coherence over long distances is determined solely by the residual thermal excitation of phononic long-wavelength phase fluctuations. The number of phonons in the specific modes follows a phonon statistics. It can be shown analytically that the presence of these phonons is expected [14, 42] to cause the coherence  $g^{(1)}$  between  $\mathbf{r}_1 = (x; y)$  and  $\mathbf{r}_2 = (-x; y)$  to decay as a power-law (also known as

---

<sup>1</sup>Actually, the entropy of a bound pair is slightly larger than the entropy of a single vortex. The number of positions at which a free vortex can be is equal to the number of positions at which the vortex of a vortex-antivortex pair can be. However in the case of a pair, for each possible position of the vortex, there are several different possible positions for the bound antivortex.

“algebraically”) of the form

$$g^{(1)}(x, -x) = \frac{n_s}{n} \left( \frac{|x|}{\Lambda} \right)^{-a_p} \quad (3.9)$$

where  $n_s$  and  $n$  are the superfluid and total densities,  $\Lambda$  is a characteristic length of the order of the healing length  $\xi$  and the exponent is

$$a_p = \frac{1}{n_s \lambda_T^2}. \quad (3.10)$$

The algebraic coherence decay can also numerically be simulated (appendix C). This power-law decay of  $g^{(1)}$  is specifically a result of the density of states for phonons in a 2D system [42, 46], and it differs distinctly from the three-dimensional BEC state where the correlation function approaches a constant value at large distances [36].

### 3.3.5 BKT transition

The transition between the state with free vortices and the BKT state where only bound vortex-antivortex-pairs exist is known as the BKT transition (figure 3.2). If one starts with a system with  $n_s \lambda_T^2 < 4$ , it contains free vortices and therefore no spatial coherence exists over long distances. Now if one increases the superfluid density  $n_s$  (or decreases the temperature which leads to an increase of  $\lambda_T$ ), eventually  $n_s \lambda_T^2$  will exceed 4. As soon as this happens, all the vortices will bind in vortex-antivortex-pairs, forming the BKT state (figure 3.3). Since the bound pairs do not affect the spatial coherence over long distances, the correlation function in the BKT state is only affected by the thermally excited phononic phase fluctuations, which cause it to decay with a power-law.

It is noteworthy that the exponent of the power-law is simply the reciprocal of the quantity  $n_s \lambda_T^2$ , and that the BKT state can only exist when this  $n_s \lambda_T^2$  quantity

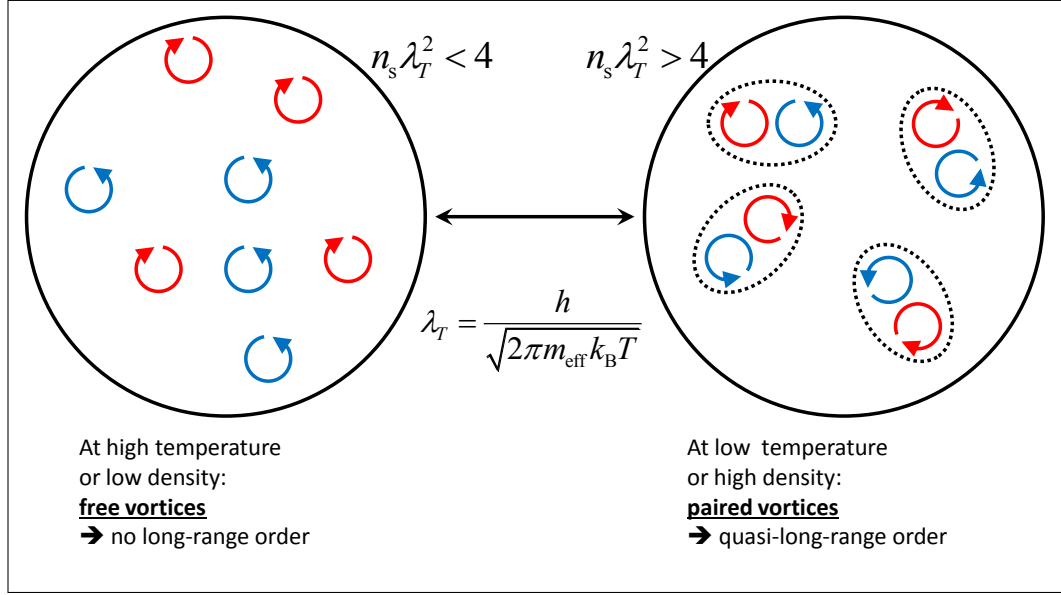


Figure 3.2: BKT transition between free vortices (left) and bound vortex-antivortex pairs (right).

is at least 4. This means the maximum possible exponent is  $a_p = \frac{1}{4}$  (at the BKT threshold). It is one of the main conclusions of the BKT theory [40, 41], that at threshold the coherence always algebraically decays with an exponent of exactly  $\frac{1}{4}$ , independent of which physical system one observes [47, 48]. If  $n_s \lambda_T^2$  is increased to even higher values, the exponent  $a_p = \frac{1}{n_s \lambda_T^2}$  will continually decrease to values of less than  $\frac{1}{4}$ . However a power-law with an exponent of more than  $\frac{1}{4}$  is not possible under this theory since this would require a  $n_s \lambda_T^2$  of less than 4 which leads to the creation of free vortices which destroy the coherence so that no power-law can be observed.

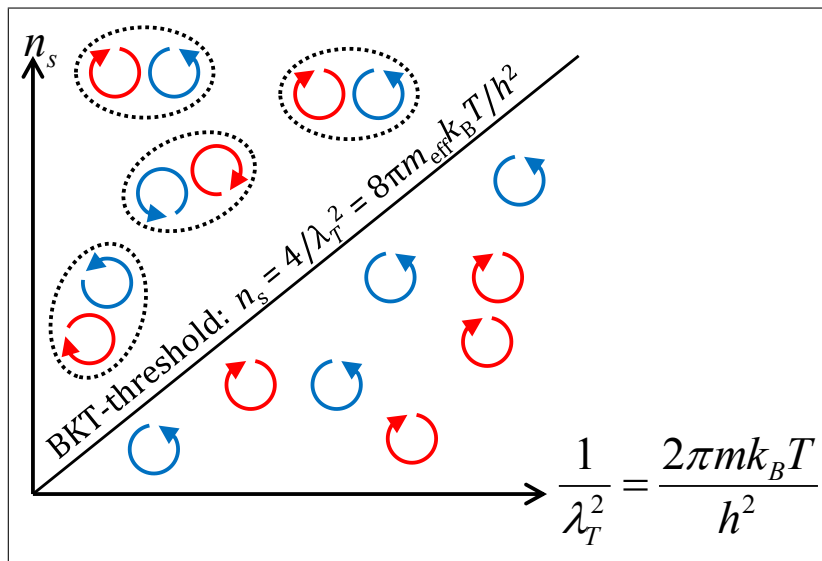


Figure 3.3: Diagram of BKT transition. At high superfluid density  $n_s$  and low temperature  $T$ , only vortex-antivortex-pairs exist and spatial coherence is possible over long distances. Decreasing  $n_s$  or increasing  $T$  causes the system to cross the BKT threshold where the vortices unbind, and by doing this they destroy the spatial coherence.

# Chapter 4

## Sample

The sample <sup>1</sup> (figure 4.1) used for these measurements consists of quantum wells in



Figure 4.1: Pieces of the sample (glued to the copper sample holder)

a cavity which is surrounded by mirrors on its top and bottom. It consists of many semiconductor layers (figure 4.2), which have been epitaxially grown onto a GaAs substrate. First, 24 pairs of AlAs and AlGaAs layers have been grown onto the substrate. Since the index of reflection  $n$  of GaAs is different from that of AlGaAs, these layers

---

<sup>1</sup>sample number M3531-7

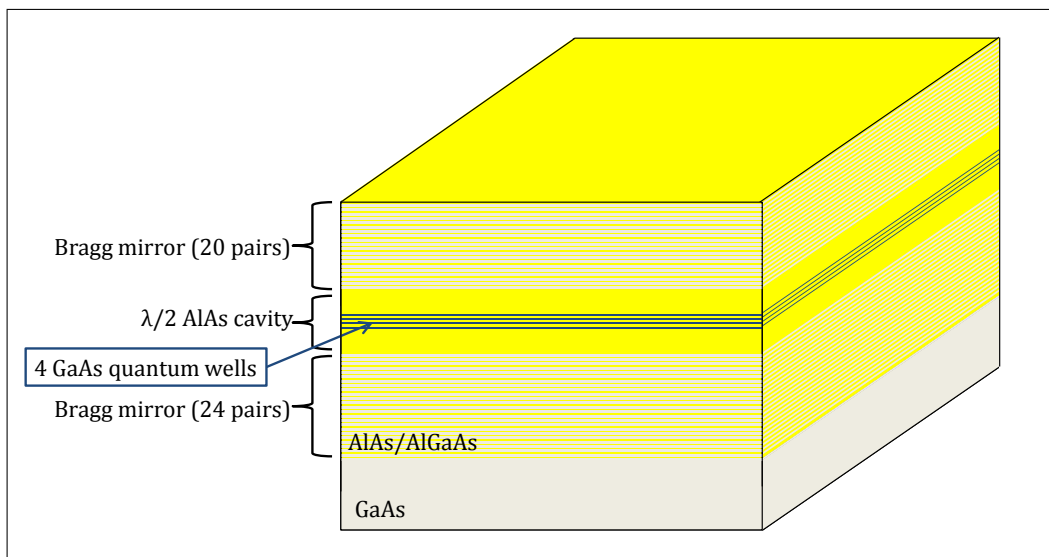


Figure 4.2: Structure of the sample

act as a distributed Bragg reflector (DBR). The thicknesses of the individual layers (65 nm for AlAs and 56 nm for AlGaAs) have been chosen in such a way that the light reflected at all the interfaces between the different layers interferes constructively.

An AlAs  $\lambda/2$  cavity with a total of four GaAs quantum wells has been grown on top of the distributed Bragg reflector. Each quantum well is 7 nm thick, and they are separated from each other by 4 nm AlAs layers. To maximize the interaction between cavity photons and quantum well excitons, the quantum wells have been positioned close to the center of the cavity, where the standing light wave reaches its maximum amplitude. Finally, a second DBR consisting of 20 AlAs/AlGaAs pairs has been grown on the top of the sample.

Having multiple quantum wells in the cavity is helpful to increase the coupling between cavity photons and quantum well excitons, since the Rabi splitting is proportional to the square-root of the number of quantum wells [3, 49, 50]. Using many quantum wells also decreases the number of exciton-polaritons per quantum well, and this is helpful to avoid unintended VCSEL lasing which can happen once the density

of exciton-polaritons in any individual quantum well is sufficient to create a population inversion. The sample is installed in a helium flow cryostat which keeps the temperature typically at  $\approx 5$  K.

## 4.1 Position dependent detuning

The sample has been intentionally produced in such a way that the thickness of the cavity slightly changes with position, meaning that the cavity has a wedge form. As a result of this, the resonant energy of the cavity photons also changes with position, whereas the energy of quantum well excitons is independent of the position. Therefore the detuning depends on the position (table 4.1), and for measurements one can choose a spot of the sample where the detuning has the desired value.

## 4.2 Experimental characterization

The sample can be experimentally characterized by shining white light onto it and performing energy and momentum resolved measurements (figure 4.3) of the reflected photons [51]. The energy resolution is achieved by a grating in the spectrometer <sup>2</sup>, whereas the in-plane momentum of the decaying excitons can be calculated from the angle at which the photons leave the sample. The energy of the upper and lower polaritons can be determined from the lowest point of their respective parabolas (at  $k = 0$ ), and the form of the parabolas shows their respective effective masses (figure 4.5). These measurements show that the Rabi splitting, which is equal to the energy difference at zero detuning between upper and lower polariton is approximately 10 meV in the used sample with four quantum wells. These measurements also allow the determination of the cavity  $Q$ -factor, which determines the lifetime of the cavity

---

<sup>2</sup>resolution up to 0.02 meV

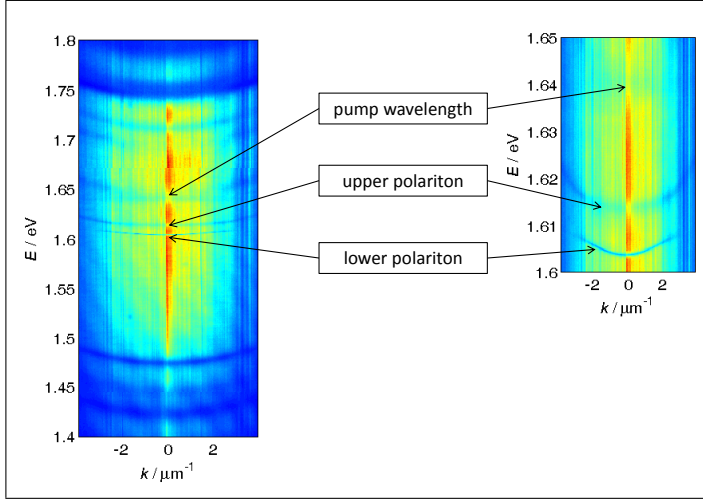


Figure 4.3: Momentum and energy resolved measurement of the reflected white light. The lines corresponding to upper and lower polariton are clearly visible. One also sees several parabolas outside of the stop-band; these correspond to wavelengths where the Bragg reflector is not efficient.

photons and therefore also of the exciton polaritons. This  $Q$  factor can be measured (figure 4.4) in the far red detuned region of the sample, where the lower polariton is essentially the same as a photon. It can be calculated as

$$Q = \lambda_0 / \Delta\lambda \approx 3000, \quad (4.1)$$

where  $\lambda_0$  is the central wavelength (at  $k = 0$ ) of the lower polariton parabola, and  $\Delta\lambda$  is the full width at half maximum of its signal (again at  $k = 0$ ). From this, the cavity photon lifetime can be calculated as

$$\tau_{\text{cav}} = \frac{2Q}{\omega_{\text{cav}}} = \frac{Q\lambda_0}{\pi c}. \quad (4.2)$$

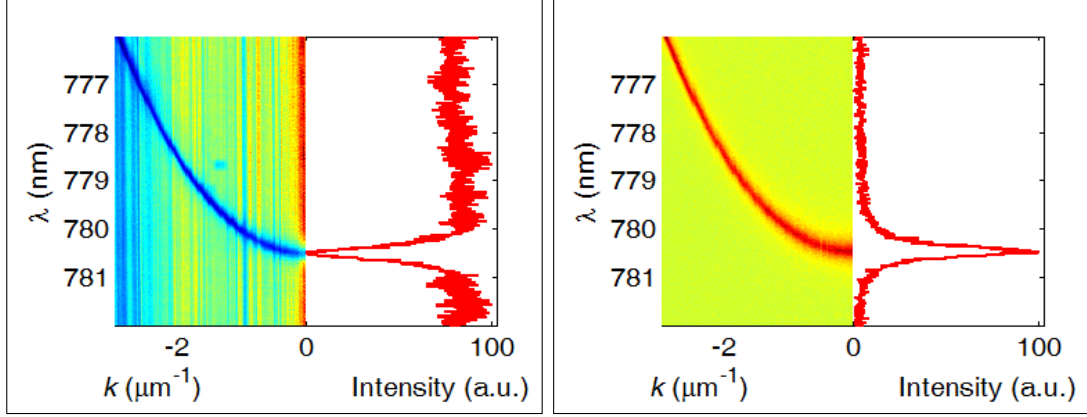


Figure 4.4: Determining the  $Q$ -factor (here:  $Q \approx 3000$ ) from the full width at half maximum (FWHM) of the white-light reflection signal (left). The same data can also be determined from photoluminescence data (right).

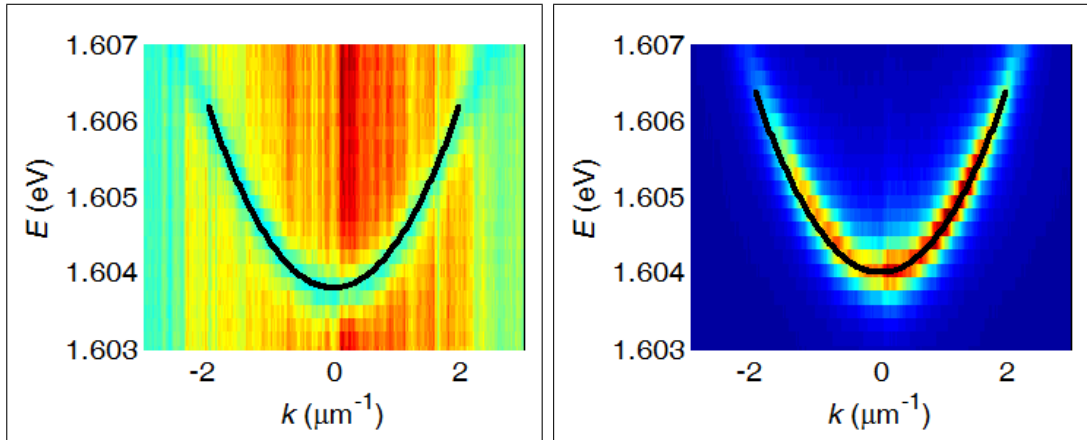


Figure 4.5: Determining  $m_{\text{LP}}$  and  $E_{\text{LP},0}$ : The effective mass  $m_{\text{LP}}$  (here:  $5.7 \times 10^{-35}$  kg) and energy  $E_{\text{LP},0}$  (here: 1.604 eV) can be determined by fitting a function of the form  $E_{\text{LP}}(k) = E_{\text{LP},0} + \frac{\hbar^2 k^2}{2m_{\text{LP}}}$  to the measured dispersion data. This measurement can be done with white light reflection (left) or by exciting at a higher energy and measuring the photoluminescence (right). The same evaluation can also be done for the upper-polariton (UP) and for the parabolas outside of the stop band.

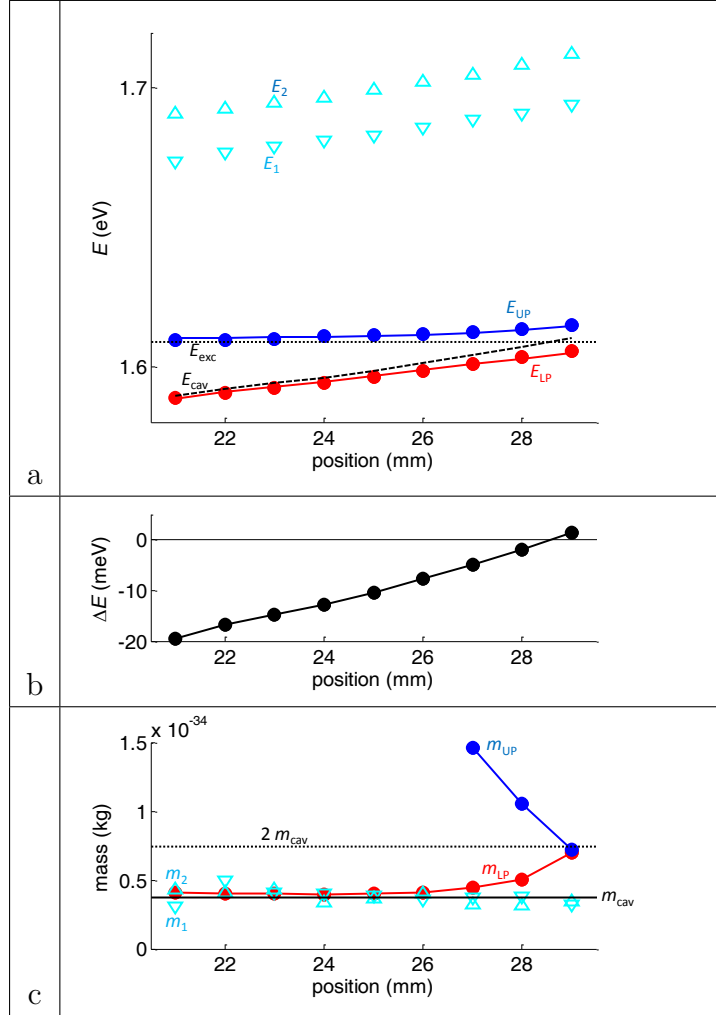


Table 4.1: Position (or detuning) dependence of the energy levels and effective masses. (a) Measured energies for lower polariton ( $E_{LP}$ ), upper polariton ( $E_{UP}$ ) and the first two reflection minima outside of the stop band ( $E_1$  and  $E_2$ ). The horizontal dotted line is the fitted exciton energy ( $E_{exc}$ ) and the dashed black line is the fitted cavity energy ( $E_{cav}$ ). The fit gives an quantum well exciton energy of  $E_{exc} \approx 1609$  meV and a Rabi splitting of  $2g_0 \approx 10$  meV. For the fits, it has been assumed that the energy difference between the parabolas outside of the stop-band and the cavity energy is constant.

(b) The detuning  $\Delta E = E_{cav} - E_{exc}$  as determined by the fit in (a).

(c) The effective masses of lower polariton, upper polariton and the two reflection minima outside of the stop band. The horizontal lines are the fit result for the effective photon mass  $m_{cav}$  (which has been assumed to be equal to the effective mass of the reflection minima outside of the stop band) and for  $2m_{cav}$ . As expected, at zero detuning one notices  $m_{LP} \approx m_{UP} \approx 2m_{cav}$ .

# Chapter 5

## Experimental setup

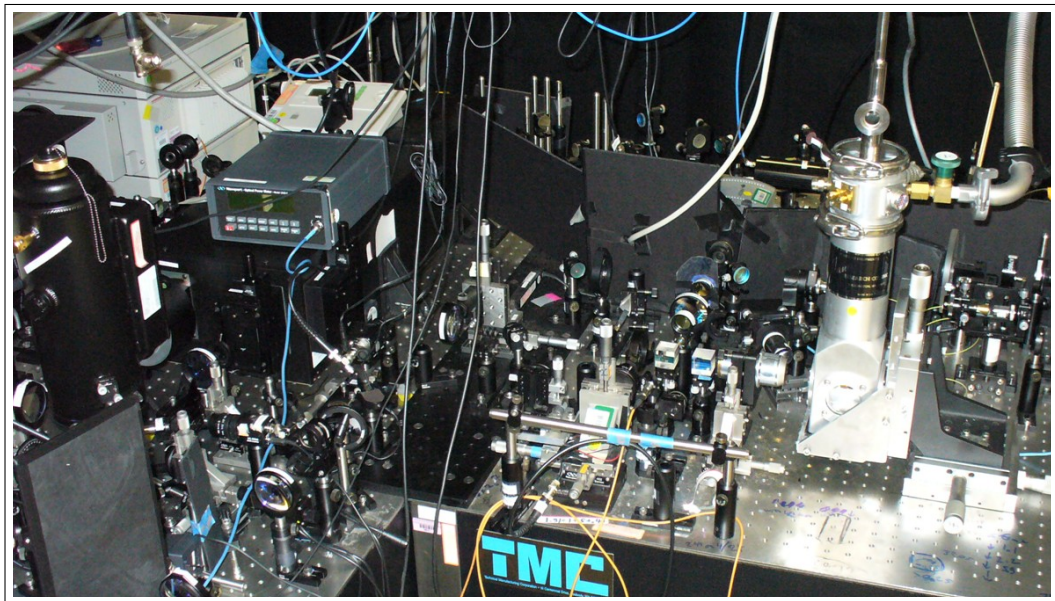


Figure 5.1: Photo of the experimental setup

The used setup allows us to perform optical measurements on the sample. For this, the sample is kept in a cryostat. We excite the sample (and create exciton-polaritons) by shining laser light onto it. Alternatively, white light can be reflected from the sample for some characterizations. The detection part of the setup collects

the photons which leave the sample and is used to analyze them.

## 5.1 Cryostat

The sample is kept under vacuum in a helium flow cryostat. It is glued onto a copper sample holder, which through a steady liquid helium flow can be kept at a temperature of around 5 K. The cryostat has transparent glass windows, which allow the optical excitation of the sample as well as the collection of the light which is emitted by the sample. The cryostat also has a built-in electric heater which can be used if a higher sample temperature is desired.

## 5.2 Optical pump (for creating exciton-polaritons)

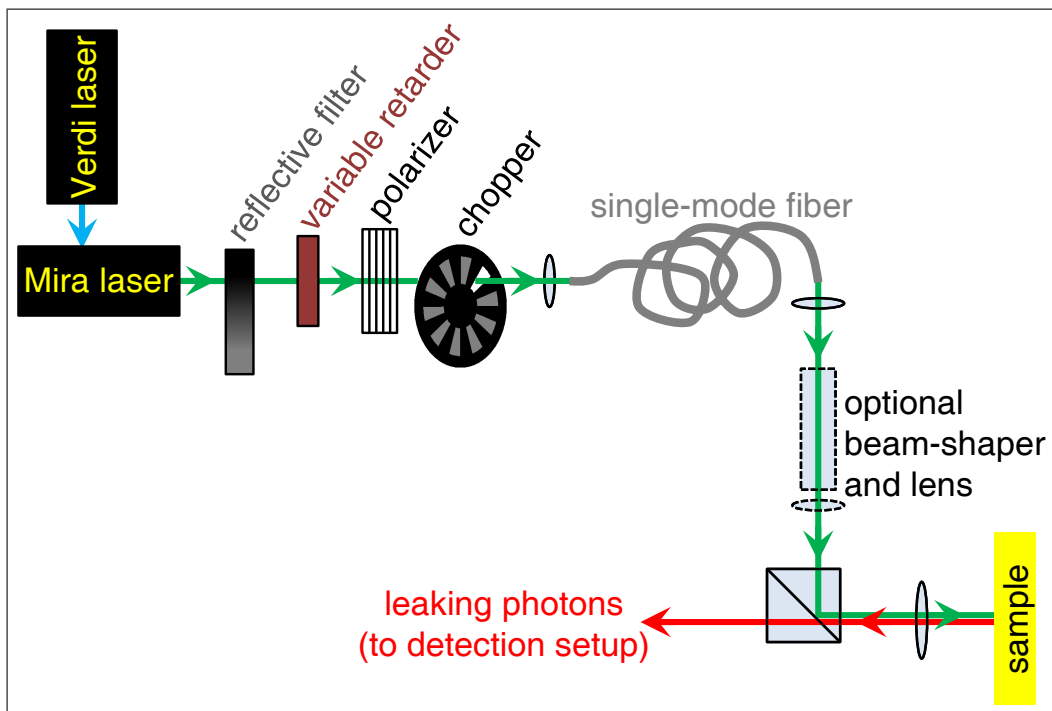


Figure 5.2: Setup of the optical pump for creating exciton-polaritons.

We create an exciton-polariton condensate by pumping non-resonantly the sample with perpendicular incidence by a Ti:Sapphire laser in continuous-wave (CW) operation. This means the pump wavelength is shorter than the cavity resonant wavelength, and is chosen to coincide with a reflection minimum outside the Bragg reflector stop band so that the pump light can efficiently reach the quantum wells where it creates electron-hole pairs (figure 4.3). These hot electron-hole-pairs cool down by multiple scattering events until they form an exciton. An additional benefit of this is that they lose the coherence which they might initially acquire from the coherent laser-pump; so if the exciton-polaritons later display coherence, it must be a result of condensation instead of an artifact caused by the coherence of the excitation [4,52].

### 5.2.1 Laser

The sample is optically excited by light from a Coherent Mira Ti:Sapphire laser. This laser is capable of emitting pulsed light; however for the excitation of the sample it is used in continuous wave (CW) mode <sup>1</sup>. The Mira laser itself has a wavelength dependent output power of around 0.5 - 1 W, and is pumped with around 8 W green laser light from a Coherent Verdi laser.

### 5.2.2 Control of laser power

The power of the laser light is attenuated to the desired level by a reflective filter and a combination of a variable retarder with a polarizer.

---

<sup>1</sup>Pulsed excitation usually results in a lower threshold pump-power for reaching the condensation threshold of the exciton-polaritons. A few measurements with pulsed excitation indicated that the behavior of the spatial coherence of the exciton-polariton condensate seems to be nearly the same as in the case of CW excitation. Therefore measurements with pulsed excitation are not discussed in this thesis.

**Reflective filter** The reflective filter is a piece of glass with reflective metal coating; the thickness of the coating and therefore the reflectivity changes with position. This means the laser power after this filter can be adjusted by moving a part with a higher or lower reflectivity of the filter into the beam path.

**Variable retarder** Additionally, the laser power can also be attenuated using the variable retarder. This retarder consists of a liquid crystal which rotates the polarization of the linearly polarized laser light. The angle at which the polarization is rotated depends on the electrical voltage which is applied to the liquid crystal. Afterwards, the light is sent through a polarizer where only the horizontal polarized component of the light passes through. This allows automated power dependent measurements, since the voltage applied to the liquid crystal can be computer-controlled.

### 5.2.3 Chopper

To avoid thermal heating, the laser is chopped at 100 Hz with a duty-cycle of 5 % so that during each 10  $\mu$ s period the pump laser only hits the sample for 0.5  $\mu$ s, which is still much longer than the exciton-polariton lifetime, so that CW excitation is guaranteed. The chopper which is used for this is a rotating wheel which lets the laser beam through its window for 5 % of the time, but for the remaining 95 % of the time blocks the beam path.

### 5.2.4 Single mode fiber

Afterwards the light is coupled into a single mode fiber. This fiber improves the spatial form of the pump beam, since after leaving the fiber, the laser beam has been forced into a Gaussian spatial intensity profile, independent of what its exact form might have been initially. Typically only around 50 % of the incoming light is

successfully coupled into the fiber, and the coupling efficiency depends on the exact form and direction of the incoming laser beam. This means if the incoming laser beam has spatial fluctuations (for example because temperature fluctuations of the air in the beam path), also the power which is successfully coupled into the fiber fluctuates and as a trade-off for the better spatial form, the fiber results in higher temporal power fluctuations.

### 5.2.5 Beam shaper

After the pump light leaves the single mode fiber, it has a Gaussian spatial intensity profile. It can optionally be sent through a beam shaper which converts its shape to a top-hat profile. Such a top-hat profile is characterized by having a nearly constant intensity within the circular area of the beam, and a negligible intensity outside of this area. If the beam shaper is not used, the pump beam maintains its slowly decreasing Gaussian form.

### 5.2.6 Polarizing beam splitter

The pump light is horizontally <sup>2</sup> polarized and it is directed towards the sample by a polarizing beam splitter.

### 5.2.7 Objective lens and pump spot size

The pump light is focused onto the sample by an objective lens with a focal length of  $f_{\text{objective lens}} = 4 \text{ mm}$ . In theory, one could increase the size of the pump spot on the sample by intentionally misaligning this lens. However the objective lens is also used to collect for further evaluation the light coming from the sample, and it has to stay

---

<sup>2</sup>We define the polarization as the direction of the electric field vector, although for historical reasons some authors continue to use the direction of the magnetic field to describe the polarization of visible light.

focused. Therefore the size of the pump spot is increased by intentionally aligning the lens after the fiber in such a way that the light is not collimated, or by adding lenses after the beam shaper. Both of these are only in the pump path and therefore do not affect the detection of the light leaving the sample.

### 5.2.8 Collecting emitted light

The emitted light from the sample is collected by the same objective lens which is also used for pumping the sample optically. Afterwards it is sent to the polarizing beam splitter, where only the vertical polarized component passes through. This design has the advantage that it filters out most of the scattered laser light. The goal is to detect the light which is emitted by the sample, but a certain fraction of the pump laser is reflected at the sample surface and other interfaces. This scattered light typically maintains the horizontal polarization of the pump laser, and therefore it is efficiently removed by the polarizing beam splitter. If we assume that the light emitted by the sample has an arbitrary polarization, around half of it will be lost at the polarizing beam splitter, since only the horizontal component passes through. This also implies that with this specific setup, the information about the initial polarization of the emitted light is lost.

## 5.3 White light reflection

For characterizing the sample it is often desirable to shine white light onto it and to analyze the reflected light. For this, the white light is produced by an incandescent lamp and brought to the setup through a multi-mode fiber (figure 5.3). After leaving the fiber, it is collimated and directed towards the sample through a non-polarizing beam-splitter. Afterwards it is focused onto the sample by the 4 mm objective lens and the reflected part of the light is again collected by the same objective lens, and after

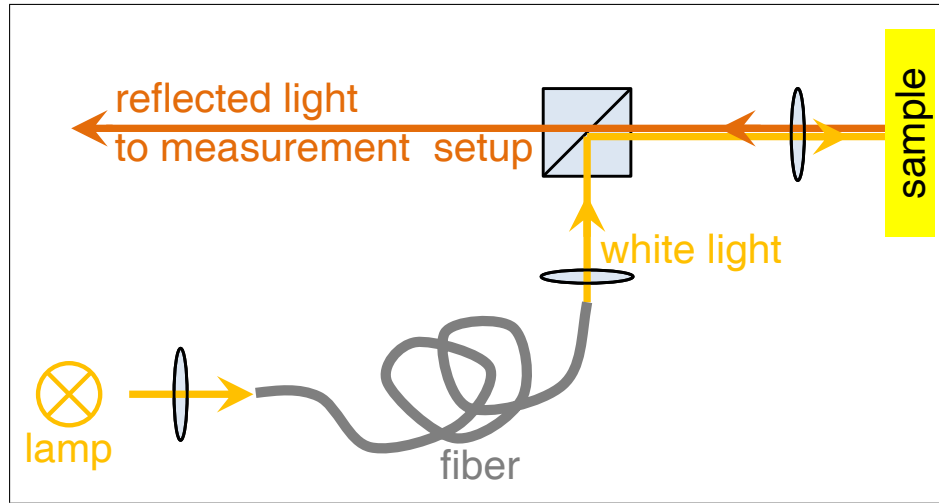


Figure 5.3: Setup for shining white light onto the sample

passing through the non-polarizing beam-splitter, it can be detected and evaluated. Using a non-polarizing beam-splitter means that half of the incident light is lost at it, and another half of the reflected signal light is also lost.

## 5.4 Position-, momentum-, and energy-resolved measurement

### 5.4.1 $x, y$ resolved

For a position resolved measurement, the light leaving the sample is collected by the objective lens and projected with another lens ( $f_{\text{before spectrometer}} = 150 \text{ mm}$ ) onto the slit of a spectrometer. This means the signal reaching the spectrometer is position ( $x$  and  $y$ ) resolved and magnified by a factor of  $m = \frac{f_{\text{before spectrometer}}}{f_{\text{obj}}} = \frac{150 \text{ mm}}{4 \text{ mm}} = 37.5$ . The spectrometer contains a grating which is used to direct the light onto a CCD camera. For a  $x$  and  $y$  resolved measurement, the slit of the spectrometer is widely opened to let the entire signal through and the grating is aligned in such a way (0<sup>th</sup>

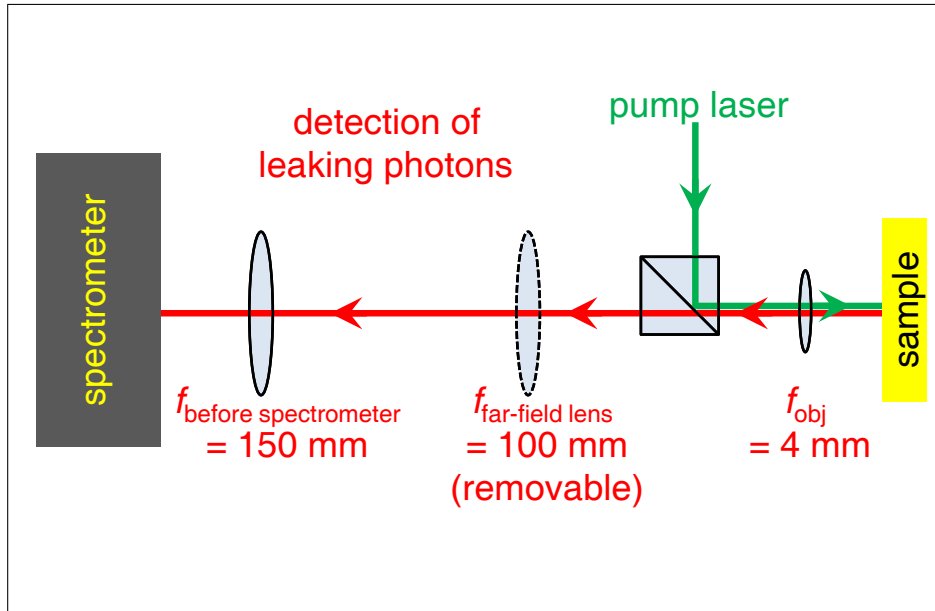


Figure 5.4: Setup for position-, momentum-, and energy-resolved measurement (with removable far-field lens)

order) that it works as a mirror and simply sends the  $x$  and  $y$  resolved image to the CCD camera. In this case, the CCD camera records a position ( $x$  and  $y$ ) resolved image, which is often called the near-field image.

### 5.4.2 $x$ , $E$ resolved

The same setup can also be used for making a position  $x$  and energy  $E$  resolved measurement. In this case, the entrance slit is nearly completely closed, so that only the part of the light with  $y \approx 0$  enters the spectrometer. In addition to this, the grating is aligned in such a way that it reflects the light in the 1<sup>st</sup> interference order which transforms the one-dimensional position  $x$  resolved signal into a position  $x$  and energy  $E$  resolved signal which is recorded by the CCD camera.

### 5.4.3 $k_x, k_y$ resolved

By adding the far-field lens (figures 5.4 and 5.5) into the beam-path, a momentum resolved image [52] is projected onto the spectrometer slit. In this case, the objec-

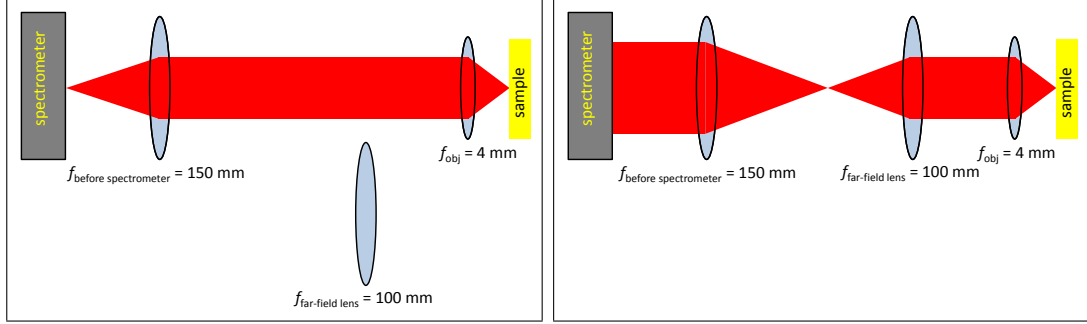


Figure 5.5: Influence of the far-field lens. With no far-field lens (left) an position resolved image is recorded, whereas with the far-field lens (right), a momentum resolved image is recorded.

tive lens and the far-field lens create a real image (magnified by  $m = \frac{f_{\text{far-field lens}}}{f_{\text{obj}}} = \frac{100 \text{ mm}}{4 \text{ mm}} = 25$ ) which is then Fourier transformed by the final lens before the spectrometer. This means the position at which a photon reaches the spectrometer entrance slit depends on the angle at which it leaked out of the sample, and this angle is approximately proportional [4] to the in-plane momentum  $\mathbf{k} = (k_x; k_y)$  of the decaying exciton-polariton which emitted the photon. With the spectrometer slit widely open and the spectrometer grating aligned to act as a simple mirror (0<sup>th</sup> order), the CCD camera records the momentum  $k_x$  and  $k_y$  resolved signal.

### 5.4.4 $k_x, E$ resolved

By nearly closing the slit so that only the signal corresponding to  $k_y \approx 0$  passes through, and aligning the grating (1<sup>st</sup> order) to send a spectrally resolved signal to the CCD camera, one can record the momentum  $k_x$  and energy  $E$  resolved signal. In this case, the resolved momentum  $k_x$  is essentially the same as the total in-plane

momentum  $\mathbf{k}$  since only photons with  $k_y \approx 0$  are detected.

## 5.5 Coherence measurement ( $x, y$ resolved)

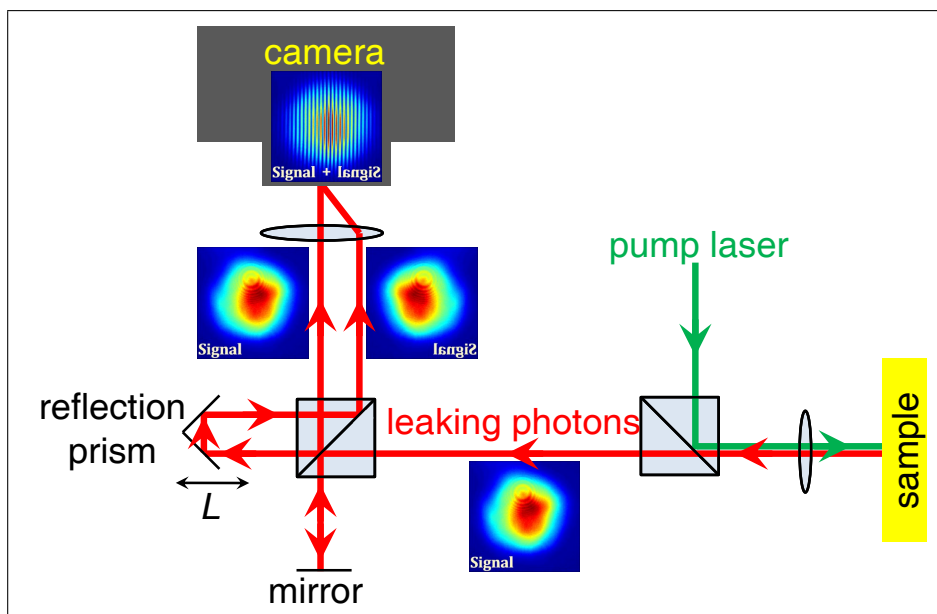


Figure 5.6: Michelson interferometer setup to measure the phase and the fringe visibility ( $x, y$  resolved)

After passing through the polarizing beam splitter, the coherence properties of the emitted light can be analyzed. For this, a Michelson interferometer with a variable path-length difference  $L$  is used [14]. After being collected by the objective lens, the component of the emitted light which is polarized perpendicular to the pump beam passes through the polarizing beam-splitter and reaches the Michelson interference setup. There it is divided by a non-polarizing beam splitter into the two arms of the interferometer.

### 5.5.1 First arm

The light which travels through the first interferometer arm is reflected by a mirror and afterwards it is sent to a CCD camera.

### 5.5.2 Second arm

In the second arm, the light is reflected by a reflection prism which flips the image along the  $y$ -axis before directing it to the camera <sup>3</sup>. Therefore at the camera the light which is emitted at point  $(x; y)$  of the sample and travels through the first arm interferes with the light from point  $(-x; y)$  coming through the second arm. The

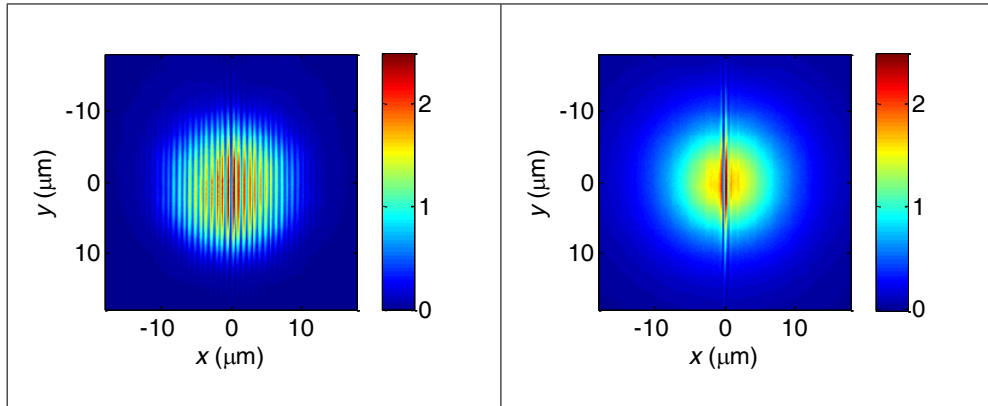


Figure 5.7: Measured interferogram (with intensity in arbitrary units) for one specific path-length difference  $L$ , measured at a pump-power above condensation threshold (left; same measurement as left column of figure 7.3) and below condensation threshold (right) where no spatial coherence exists over long distances.

prism is aligned in such a way that the path length through both interference arms is nearly the same <sup>4</sup>. The prism is mounted with a piezo in such a way that it can

<sup>3</sup>Strictly speaking, the light in the interference setup is in momentum space since it has been Fourier transformed by the objective lens. This means by flipping it around in the prism, initially  $k_x$  is replaced by  $-k_x$ . Afterwards, the lens before the camera performs the inverse Fourier transform from momentum to position space, where now  $x$  has been replaced by  $-x$ .

<sup>4</sup>This means that only the coherence between photons which left the sample approximately at the same time is measured. By choosing significant different path lengths, it is possible to measure temporal coherence, although this has not been used for this work.

be moved by up to  $\approx 1 \mu\text{m}$ . This allows to slightly change the path length difference and therefore the relative phase of photons traveling through the different arms.

### 5.5.3 Interference signal at the CCD camera

The wave-fronts from the two arms reach the camera at a slightly different angle which gives rise to interference fringes. Scattered light from the pump laser is filtered out by band-pass filters before reaching the camera. The piezo is used for slightly moving the prism, and the interferogram (figure 5.7) is recorded for many different path-length differences.

## 5.6 Data evaluation

The measured intensity of each of the pixels (corresponding to a position  $(\pm x; y)$  on the sample) as a function of the change  $\Delta L$  of the path-length difference  $L$  follows a sine law (figure 5.8) of the form  $I_{\text{measured}}(\Delta L) = B + A \sin(K\Delta L - \varphi_0)$ . As explained

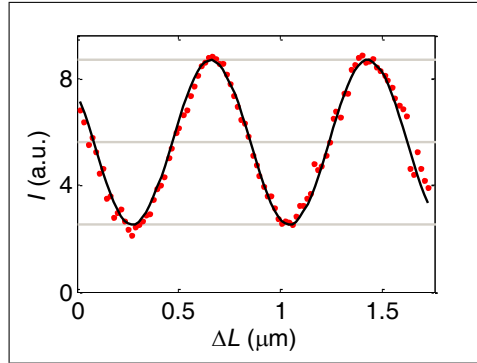


Figure 5.8: The intensity of each pixel behaves like a sine function of the form  $I_{\text{measured}}(\Delta L) = B + A \sin(K\Delta L - \varphi_0)$  if plotted as a function of the change  $\Delta L$  of the path-length difference  $L$ .

in appendix A, the first order correlation function  $g^{(1)}(x, -x)$  is identical to the visibility  $V(x)$  and can therefore be calculated as  $g^{(1)}(x, -x) = A/B$  from the fitting

parameters  $A$  and  $B$ . Doing this sine fit for each individual pixel  $(\pm x; y)$  gives both the (2-dimensional) image of the visibility  $V(x, y) = g^{(1)}(x, y; -x, y)$  and the (2-dimensional) phase map  $\varphi_0(x, y)$  as shown in figure 7.3. The phase map can be used to confirm that the long-range-order is produced and the fit was able to extract reliable data of the visibility [14], because for successfully evaluated data, the phase map shows clear fringes, whereas otherwise it looks like noise (for example noise in most of the upper right panel in figure 7.3).



# Chapter 6

## Previous work by other researchers

Bose-Einstein condensation is characterized by the macroscopic occupation of the lowest-energy state and has been observed in atomic gases [23,53] as well as with quasi-particles in solid state systems [3,4]. It is accompanied by superfluidity [32,54–56] and long-range spatial coherence [57–60]. Previously, the BKT transition has been demonstrated for superfluid liquid helium films [61,62], superconducting films [63,64] and 2D atomic gases [43]. However, the power-law decay of spatial correlations expected for the BKT phase, which is its most distinct characteristic, has never been established quantitatively. Previous measurements [14] of the coherence of an exciton-polariton condensate looked similar to a power-law decay, however both the exponent and its dependence on the pump-power were inconsistent with the predictions of the BKT theory. This thesis shows that the measured first-order spatial correlation function of an exciton-polariton condensate decays with a power-law, whose exponent is  $\approx \frac{1}{4}$  at the condensation threshold, as predicted by the BKT theory. Recent theoretical work [65] confirmed that the continuous creation and decay of exciton-polaritons does not prevent our finite-sized non-equilibrium system from exhibiting the BKT state with quasi-long-range coherence. [13]



# Chapter 7

## Measured coherence

For the measurements described in this chapter [13], we use a laser beam with a Gaussian spatial intensity profile (with a full width at half maximum of  $15\ \mu\text{m}$ ) which can only efficiently excite the lowest spatial mode of the condensate. Previous measurements [14] used a different <sup>1</sup> sample, and tried to create a uniform condensate density by using a top-hat formed pump beam. However such a top-hat pump profile can easily lead to condensate fragmentation into multiple spatio-energy modes [66]. In this case, the measured overall visibility might decay faster than the intrinsic coherence for each individual mode, since any interference between different energy modes averages out to zero during the integration time of the camera (see chapter 8 for details).

---

<sup>1</sup>The sample used for the previous work had 16 mirror pairs at the top and 20 at the bottom. It contained a total of 12 quantum wells which resulted in a Rabi splitting of  $2g_0 = 14\ \text{meV}$ . [14,66]

## 7.1 Condensation threshold and blue-shift of exciton-polariton energy

In order to create an exciton-polariton condensate one has to increase the pump-power above the condensation threshold. In Fig. 7.1, one sees that the exciton-polaritons in

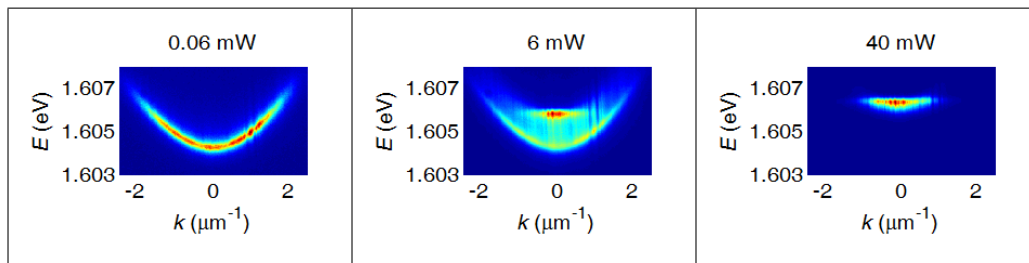


Figure 7.1: Pump-power dependent dispersion (measured at  $\delta \approx -1$  meV). At around 6 mW, the condensation phase appears, and at above this pump-power, nearly all exciton polaritons are in a ground state with approximately zero momentum and one specific energy. A blue-shift towards higher energies due to repulsive interaction between the exciton-polaritons is observed above condensation threshold.

the condensate are more energetic than those measured below condensation threshold. One also sees that above the condensation threshold <sup>2</sup> of  $\approx 6$  mW, nearly all the exciton-polaritons are in a condensed state at one single energy level and with an in-plane momentum of  $k \approx 0$ . Figure 7.2 shows the power-dependent signal which is emitted close to  $k = 0$ . A jump to shorter wavelengths at condensation threshold as well as a continuous blue-shift above threshold are the result of repulsive interaction between exciton-polaritons. The continuous blue-shift above threshold is a signature of exciton-polariton condensation since it does not appear in the case of VCSEL lasing.

<sup>2</sup>The pump power is always measured after coupling the light out of the single-mode fiber. The power which actually reaches the sample is lower due to losses on the objective lens before the cryostat and other optical components. The power is always measured while the chopper is open, so the time-averaged power which determines the heating of the sample is only  $\frac{1}{20}$  of the measured power.

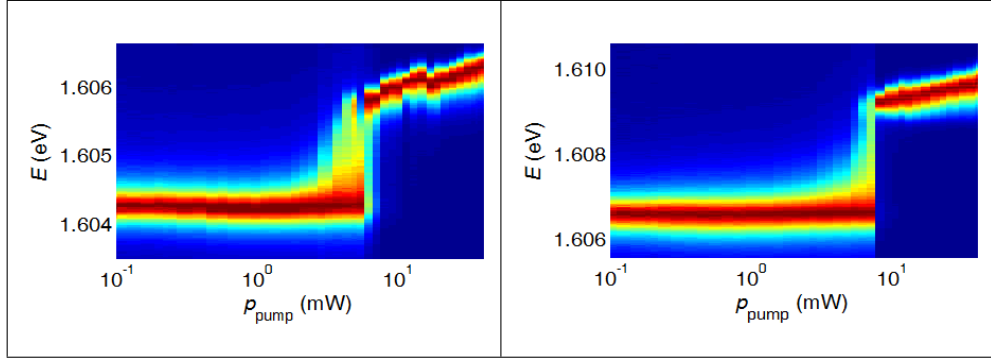


Figure 7.2: Blue-shift [25, 67] of exciton-polariton energy. Normalized signal close to zero momentum at red detuning of  $\delta \approx -1$  meV (left) and at a blue detuning of  $\delta \approx 4$  meV (right). The measurement of the exciton-polariton density (chapter 7.4.1) indicates that at the threshold of  $p_{\text{pump}} \approx 6$  mW, the total exciton polariton density is  $n \approx 2 \mu\text{m}^{-2}$ , which corresponds to an exciton-polariton density per quantum-well of  $n_{\text{per QW}} \approx 0.5 \mu\text{m}^{-2}$ . This small value confirms that we observe condensation rather than VCSEL lasing, since the later requires significant higher exciton-polariton densities of approximately  $3 \times 10^3 \mu\text{m}^{-2}$  per quantum-well to create a population-inversion.

## 7.2 Coherence

A typical result (figure 7.3, left column) for the measured phase and fringe visibility above condensation threshold shows three distinct regions:

### 7.2.1 Short distances (Region I)

The visibility over short distances (I) decays according to a Gaussian law. This is similar to the correlation function decay of a Bose gas in thermal equilibrium [36] where the width of the Gaussian is proportional to the de Broglie wavelength. However in our system the population of energetically higher modes depends primary on their overlap with the Gaussian pump profile, therefore we cannot deduce an accurate temperature from this Gaussian width [14].

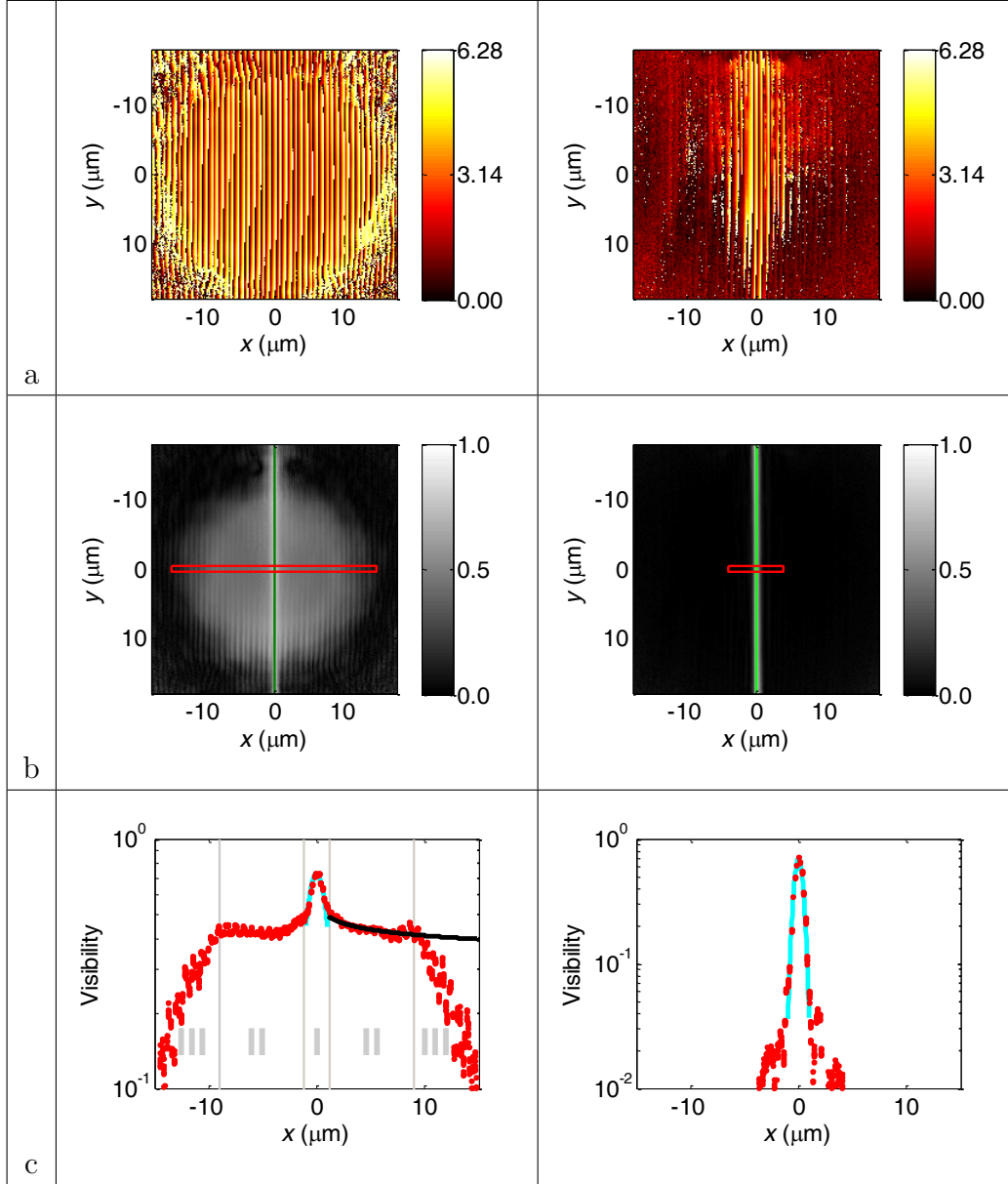


Figure 7.3: Measured phase and visibility (measured at detuning parameter  $\Delta E \approx -1$  meV; same measurement as figure 5.7). Left column: above condensation threshold (at  $p_{\text{pump}} = 15$  mW) (a) Phase map  $\varphi_0$  produced by an ensemble of pixels. (b) Visibility map. The flip-axis is shown as a line at  $x = 0$  and the region of interest used for further evaluation is highlighted by a rectangle. (c) The visibility within the region of interest as a function of the directed distance  $x$  to the flip-axis. In region II, a power-law fit with exponent  $a_p = 0.082$  is shown. The regions I, II, and III are selected manually. Right column: the same characteristics at below condensation threshold (at  $p_{\text{pump}} = 2$  mW). Absence of quasi-long-range order is clearly seen since the cyan line is a Gaussian decay function

### 7.2.2 Intermediate distances (Region II)

In the region of intermediate distances (II), the decay of the visibility follows a power law as theoretically predicted for the BKT state. From this, we determine the exponent  $a_p$  by fitting a power-law proportional to  $|x|^{-a_p}$  to the measured fringe visibility in this region.

In Fig. 7.4, three different decay functions are tested against the measured visibility. The power-law decay function gives the best match after the individual minimization of the root-mean-square deviation, which confirms that the coherence decays with a power-law, as theoretically predicted.

### 7.2.3 Very long distances (Region III)

For even larger distances (III), the visibility starts to decay much faster, which we attribute to the decrease of the superfluid fraction towards the edge of the condensate. The intensity of the Gaussian pump decreases towards the edge, which is expected to lead to a decrease [57] of the superfluid fraction  $n_s/n$ . According to equation 3.9 (and as shown in figure B.1), this picture can explain the fast drop of  $g^{(1)}$ .

## 7.3 Pump-power dependence of the exponent $a_p$

Simply by changing the pump-power  $p_{\text{pump}}$ , one can easily change both the total density  $n$  and the superfluid density  $n_s$  of the exciton-polaritons. A pump-power dependent measurement of the fringe visibility shows that, as predicted by the BKT theory, the exponent  $a_p$  is approximately  $\frac{1}{4}$  at threshold and decreases with increasing pump-power (figure 7.5). This figure also shows that overall the exponents  $a_p$  extracted for both  $x > 0$  and  $x < 0$  are equivalent, even if each individual measurement of the visibility (as shown in figure 7.3) might appear slightly asymmetrical due

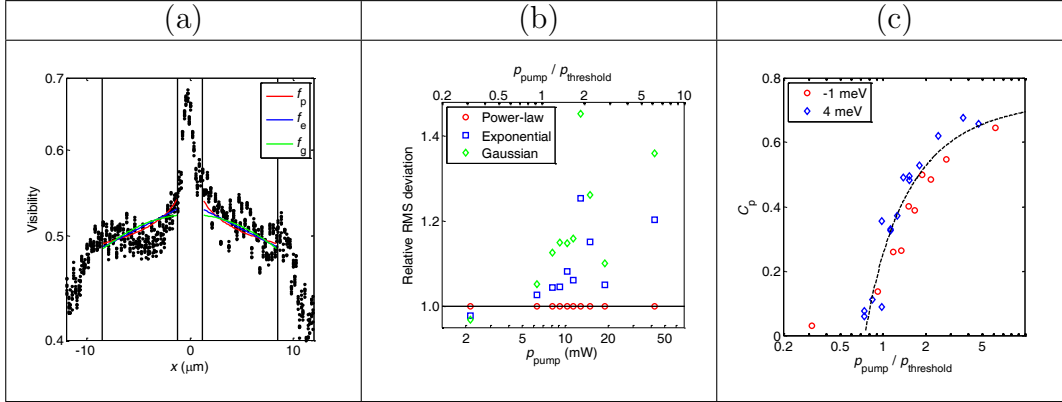


Figure 7.4: Fitting various decay functions to the visibility data.

(a) The used decay functions are a power-law of the form  $f_p(x) = c_p |x/\mu\text{m}|^{-a_p}$  (red line), exponential function  $f_e(x) = c_e \exp(-a_e |x/\mu\text{m}|)$  (blue line), and Gaussian function  $f_g(x) = c_g \exp[-a_g(x/\mu\text{m})^2]$  (green line). The fits have been performed

by minimizing the root-mean-square (RMS) deviation  $D_i = \sqrt{\sum_n [f_i(x_n) - V_n]^2 / N}$  between the fitted functions  $f_i$  (with  $i \in \{p, e, g\}$ ) and the  $N$  measured positions and visibilities  $(x_n; V_n)$  with  $x_{\min} < |x_n| < x_{\max}$ , where the limits of the intermediate range  $x_{\min}$  and  $x_{\max}$  (marked by black vertical lines) have been chosen manually. Here we use the same fit for the  $x < 0$  and the  $x > 0$  regions. The visibility shown here has been measured at  $\Delta E \approx -1$  meV and  $p_{\text{pump}} = 19$  mW.

(b) The relative RMS deviations  $R_i = \frac{D_i}{D_p}$  measured at  $\Delta E \approx -1$  meV. Above the condensation threshold, we always observed  $D_p < D_e < D_g$ , which means that the power-law decay gives the best match, and the Gaussian fit gives the worst match.

(c) The pump power dependence of the factors  $c_p$  determined by this fit at  $\Delta E \approx -1$  meV and at  $\Delta E \approx 4$  meV. The dashed line is introduced to guide the eye.

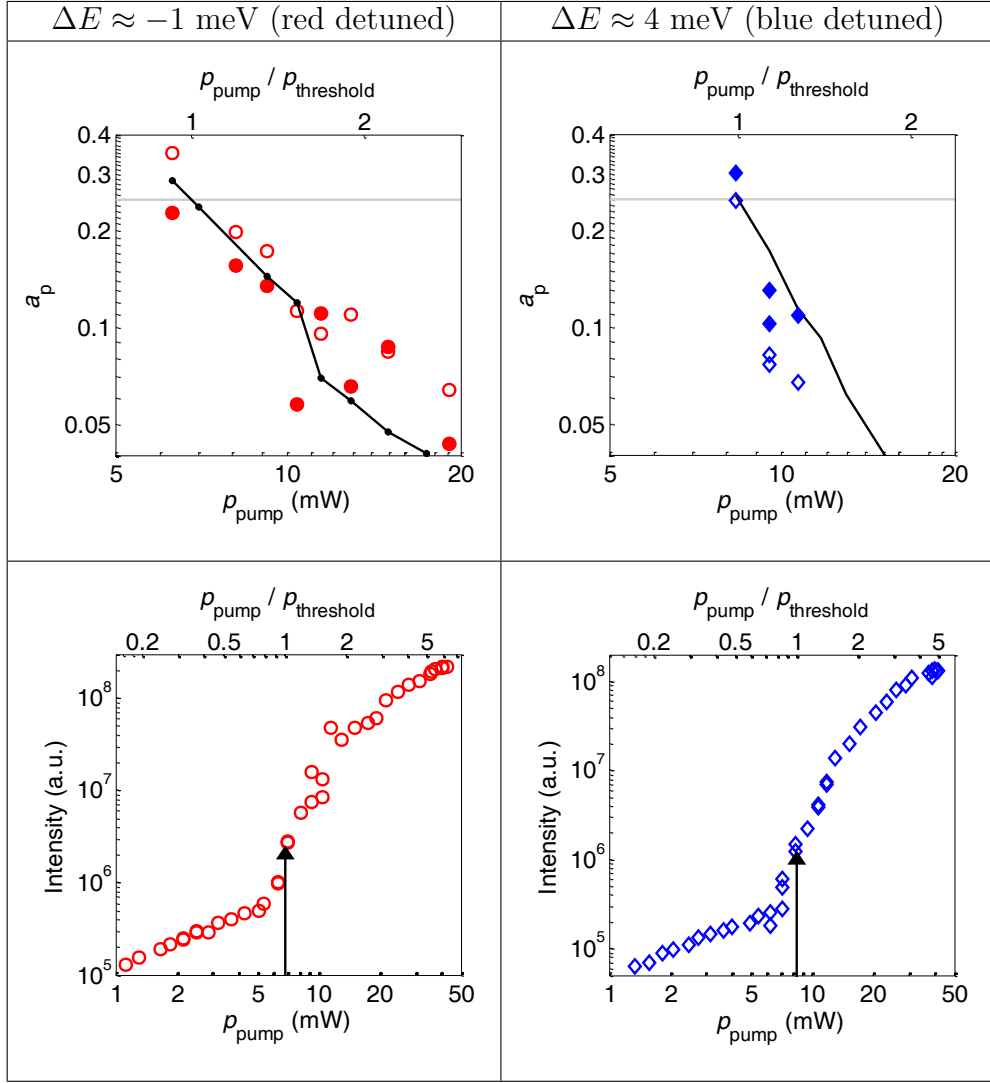


Figure 7.5: Pump-power dependence. Upper row: Pump-power dependence of the exponent  $a_p$  for two different detuning values. The symbols show the measured exponents as determined by a power-law fit as shown in figure 7.3. The grey horizontal line at 0.25 shows the theoretically predicted exponent at threshold. The black continuous line shows the estimated inverse superfluid phase-space-density  $1/(n_s \lambda_T^2)$ , and as predicted by the theory, it matches with the measured exponents  $a_p$ . Filled symbols correspond to the  $x < 0$  region. Lower row: Pump-power dependent peak intensity, as determined by an energy and momentum resolved measurement. The threshold pump-powers defined by the critical exponent  $a_p = 0.25$  (upper traces) are indicated by the black arrows.

to experimental imperfections.

## 7.4 Comparing observed exponent to predicted values

As explained previously, the exponent  $a_p$  is predicted to be identical to  $\frac{1}{n_s \lambda_T}$ .

### 7.4.1 Determination of the superfluid density $n_s$

By recording the position resolved image (figure A.1) of the condensate with a calibrated camera and estimating the transmittance  $T_{\text{path}}$  of the beam-path from the sample to the camera, we can estimate the photon flux  $j$  at which photons leak out of the sample. The exciton-polariton lifetime  $t_{\text{LP}}$  can be calculated as  $t_{\text{LP}} \approx t_{\text{cav}}/|C|^2$ , where the Hopfield-coefficient  $|C|^2$  is the detuning dependent photon component of the exciton-polariton, and the photon lifetime  $t_{\text{cav}}$  is known from the quality factor of the cavity. The 2D total exciton-polariton density is estimated as  $n = jt_{\text{LP}}$ . We know that above the threshold, the superfluid density  $n_s$  is about one half of this total density  $n$ , since the measured visibility is approximately  $\frac{1}{2}$  at the transition from region I to region II in figure 7.3.

### 7.4.2 Determination of the thermal de Broglie wavelength $\lambda_T$

#### Exciton-polariton temperature

While the sample is kept at  $\approx 5$  K, exciton-polaritons, which are not in thermal equilibrium with the lattice, have a different temperature. Their temperature can be estimated from a position  $x$  and energy  $E$  resolved measurement. By fitting a thermal distribution to the measured energy resolved population (Fig. 7.6), although

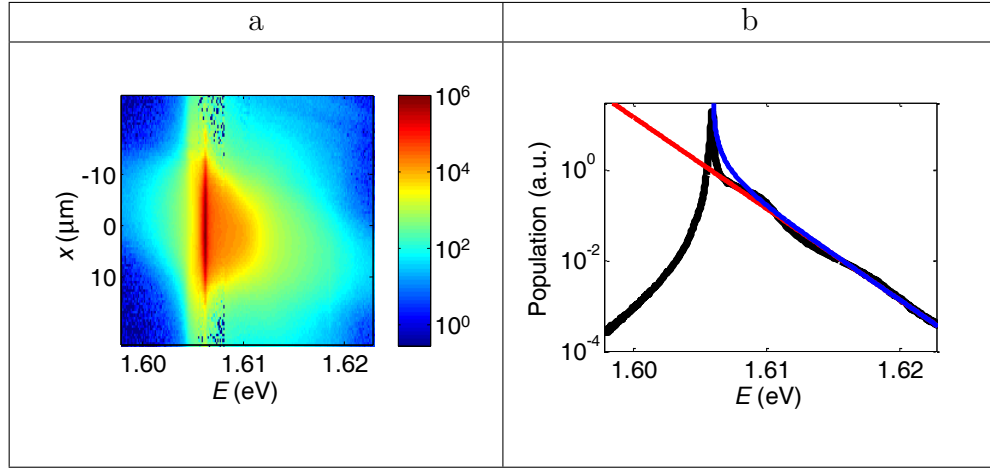


Figure 7.6: Determination of the exciton-polariton temperature.

(a) Position  $x$  and energy  $E$  resolved intensity.

(b) Measured population (black) with Boltzmann (red) and Bose-Einstein (blue) distributions for 25 K, using the data measured at  $x \approx 0$ .

the system is not in thermal equilibrium, we can estimate an effective temperature of the exciton-polaritons to be always <sup>3</sup>  $\approx 25$  K, from which we get the thermal de Broglie wavelength  $\lambda_T$ .

### Effective mass

The effective mass of the exciton-polaritons can be determined by fitting a parabola to the dispersion measured below condensation threshold (figure 4.5).

### Thermal de Broglie wavelength

Once we know the approximate temperature  $T$  and effective mass  $m_{\text{eff}}$  of the exciton-polaritons, we can calculate the thermal de Broglie wavelength as  $\lambda_T = \frac{h}{\sqrt{2\pi m_{\text{eff}} k_B T}}$ .

<sup>3</sup>The temperature determined this way seems to be nearly the same for any above-threshold pump-power.

### 7.4.3 Match between predicted and observed exponents

The continuous black line in figure 7.5 shows the calculated value for  $a_p^{\text{calculated}} := 1/(n_s \lambda_T^2)$  using these experimental values of  $n_s$  and  $\lambda_T$ , and gives a reasonable match with the experimental values for  $a_p$  from the interference measurements. In figure 7.7, we show one-to-one correspondence between the measured exponents  $a_p$  and

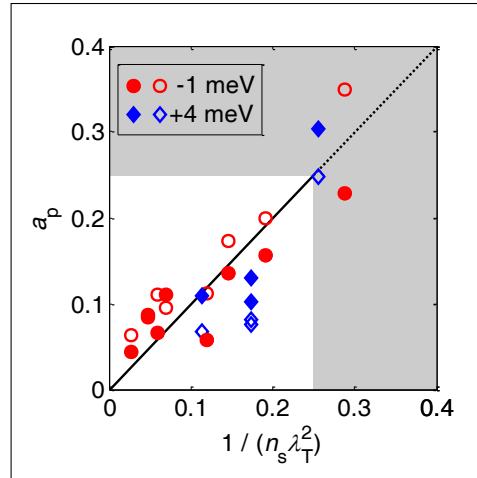


Figure 7.7: Measured exponents  $a_p$  as a function of estimated inverse superfluid phase-space-density  $1/(n_s \lambda_T^2)$ . The black line shows the predicted  $a_p^{\text{calculated}} = 1/(n_s \lambda_T^2)$ , and the region above the expected threshold of 0.25 is shaded in gray. Although we did not change the temperature during the measurement, the abscissa can be interpreted as the dimensionless temperature (in units of  $2\pi m_{\text{eff}} k_B n_s^{-1} \hbar^{-2}$ , and the BKT phase transition occurs at the dimensionless temperature of 0.25 in these units. Again, filled symbols correspond to  $x < 0$ , and different kinds of symbols to different detunings.

the phase-space density of  $1/(n_s \lambda_T^2)$ , as well as the predicted continuous line with  $a_p^{\text{calculated}} = 1/(n_s \lambda_T^2)$ . The exponents  $a_p$ , which have been measured for different pump-powers and detuning parameters, follow the predicted universal line. This observation indicates that the 2D exciton polariton condensate behaves as expected from the BKT theory.

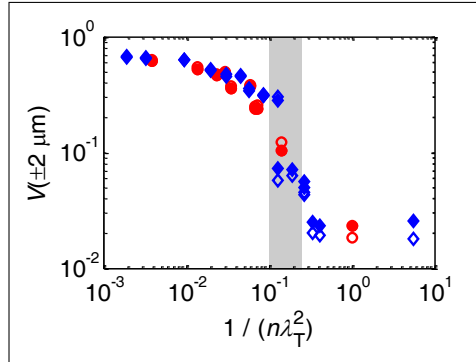


Figure 7.8: Visibility at  $x = \pm 2 \mu\text{m}$  vs. the inverse phase-space-density  $1/(n\lambda_T^2)$ . The threshold is upper bounded by  $1/(n_s\lambda_T^2) = 1/4$  and lower bounded by  $1/\ln[380\hbar^2/(m_{\text{eff}}g_{\text{interaction}})] = 1/10$ , which are shown by the shaded area. As in figure 7.5, filled symbols correspond to the  $x < 0$  region, and different kinds of symbols to different detunings.

## 7.5 Summary of exponent $a_p$ measurements

Our measurements confirm that exciton-polariton condensation can be understood not by the BEC model but exclusively within the BKT model. The measured first-order spatial coherence function fully supports a unique 2D superfluid characteristic both at and above threshold.



# Chapter 8

## Condensate fragmentation

As mentioned previously, the BKT theory predicts that the first-order spatial coherence function decays with a power-law (algebraically), whose exponent must always [42] be  $\leq \frac{1}{4}$ . This chapter shows that the spatial quasi-long-range-order of an condensate can decay faster than allowed under the BKT theory, if the system shows simultaneous condensation [66,68] into several spatio-energetic modes. This result is confirmed both by numerical simulations and by experimental measurements using an exciton-polariton system.

### 8.1 Top-hat pump profile

The sample is again non-resonantly excited by perpendicularly incident continuous-wave laser-light at a wavelength which coincides with a reflection minimum of the Bragg reflector. After leaving the single mode fiber, the incident laser beam initially has a Gaussian spatial profile, but for the measurements described in this chapter, an additional beam-shaper is used to change it to a top-hat form. The top-hat excitation is intended to create a condensate with a nearly constant density within the circular area (with radius  $R_{\text{spot}}$ ) of the excitation spot, and only a negligible density outside

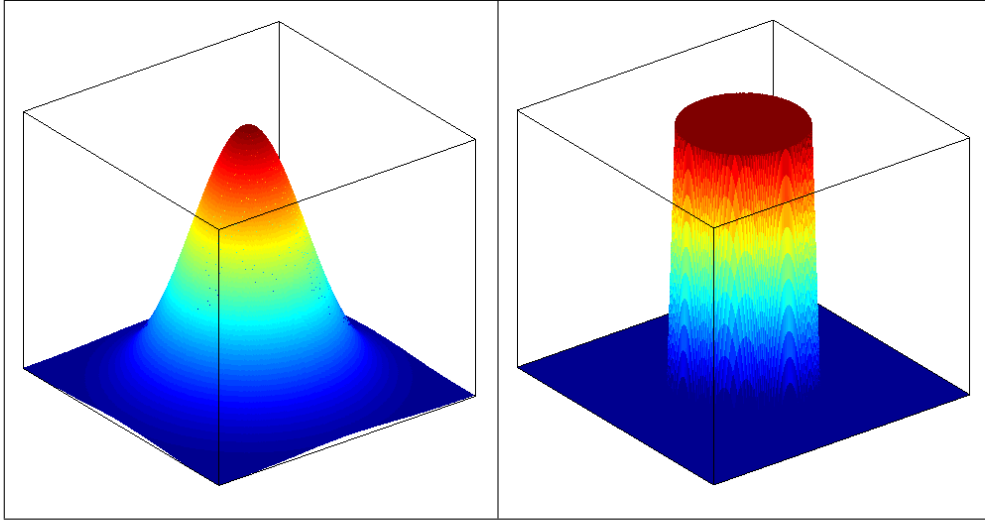


Figure 8.1: Gaussian (left) and top-hat (right) intensity profile.

of the spot.

## 8.2 Multi-mode condensation

Such a condensate with a constant density cannot be in a single quantum mechanical mode, since this would require a wave-function whose amplitude is constant within the circular area and zero everywhere else, but such a wave-function is not a solution to the Schrödinger equation. However a nearly constant total density is possible if condensation occurs simultaneously into several spatio-energetic modes  $\Psi_s$  which gives a total wave-function of the form

$$\Psi_{\text{total}}(x, y, t) = \sum_s \Psi_s(x, y, t) \quad (8.1)$$

with

$$\Psi_s(x, y, t) = A_s \psi_s(x, y) e^{\frac{itE_s}{\hbar}} e^{i\eta_s(x, y, t)}. \quad (8.2)$$

Due to the circular symmetry of the condensate, each base-function  $\psi_s$  can be expressed [66] (in polar coordinates) as

$$\psi_s(r, \phi) = J_{m_s}(k_s r) \exp(im_s \phi) H(R_{\text{spot}} - r), \quad (8.3)$$

where  $m_s$  is an integer,  $J$  is the Bessel function of the first kind, the positive  $k_s$  is chosen so that the Bessel function reaches one of its zeros at  $r = R_{\text{spot}}$ , and  $H$  is the Heaviside step function.  $E_s$  is the energy corresponding to base-function  $\psi_s$ .

The amplitudes  $A_s$  are determined by the condition that the total spatial exciton-polariton density  $n_{\text{total}}(x, y)$  has approximately the same form as the spatial intensity profile  $I_{\text{pump}}(x, y)$  of the pump laser light, which means

$$I_{\text{pump}}(x, y) \propto n_{\text{total}}(x, y) = \langle \Psi_{\text{total}}^*(x, y, t) \Psi_{\text{total}}(x, y, t) \rangle, \quad (8.4)$$

where the  $\langle \dots \rangle$  brackets indicate time-averaging. The real  $\eta_s(x, y, t)$  represents phase noise and can for example be explained by the thermal excitation of phononic long-wavelength phase fluctuations [42]. Without this phase-noise, coherence could exist over arbitrary large distances which is not possible [37, 38] in our two-dimensional system.

### 8.3 Correlation-function

The first order spatial correlation function for each individual mode  $\Psi_s$  can therefore be written (using equation 3.2) as

$$\begin{aligned} g_s^{(1)}(x_1, y_1, x_2, y_2) &= \frac{|\langle \Psi_s^*(x_1, y_1, t) \Psi_s(x_2, y_2, t) \rangle|}{\sqrt{\langle |\Psi_s(x_1, y_1, t)|^2 \rangle \langle |\Psi_s(x_2, y_2, t)|^2 \rangle}} = \\ &= |\langle \exp\{-i[\eta(x_1, y_1, t) - \eta(x_2, y_2, t)]\} \rangle|. \end{aligned} \quad (8.5)$$

The coherence of the total system  $\Psi_{\text{total}}$  can be calculated (using equations 3.2, 8.1 and 8.2) as

$$\begin{aligned} g_{\text{total}}^{(1)}(x_1, y_1, x_2, y_2) &= \frac{|\langle \Psi_{\text{total}}^*(x_1, y_1, t) \Psi_{\text{total}}(x_2, y_2, t) \rangle|}{\sqrt{\langle |\Psi_{\text{total}}(x_1, y_1, t)|^2 \rangle \langle |\Psi_{\text{total}}(x_2, y_2, t)|^2 \rangle}} = \\ &= \frac{\left| \sum_s |A_s|^2 \psi_s^*(x_1, y_1) \psi_s(x_2, y_2) g_s^{(1)}(x_1, y_1, x_2, y_2) \right|}{\sqrt{\left( \sum_s |A_s \psi_s(x_1, y_1)|^2 \right) \left( \sum_s |A_s \psi_s(x_2, y_2)|^2 \right)}}. \end{aligned} \quad (8.6)$$

Here we used

$$\begin{aligned} \left\langle \exp \left\{ -i [\eta_{s_1}(x_1, y_1, t) - \eta_{s_2}(x_2, y_2, t)] \right\} \exp \left( -i \frac{E_{s_1} - E_{s_2}}{\hbar} t \right) \right\rangle = \\ = \langle \exp \left\{ -i [\eta_{s_1}(x_1, y_1, t) - \eta_{s_2}(x_2, y_2, t)] \right\} \delta(s_1, s_2) \rangle, \end{aligned} \quad (8.7)$$

which assumes that the energies are non-degenerate, so that for  $s_1 \neq s_2$  all interference terms with  $\exp[-i(E_{s_1} - E_{s_2})t/\hbar]$  average out to zero<sup>1</sup>. Equation 8.6 shows that even if each individual mode is perfectly<sup>2</sup> coherent ( $g_s^{(1)} \approx 1$ ), the overall coherence  $g_{\text{total}}^{(1)}$  can nevertheless exhibit a fast decay, as a direct result of the simultaneous excitation of several modes  $\Psi_s$ . The details of which modes  $\Psi_s$  are excited are determined by the pump profile  $I_{\text{pump}}(x, y)$ . This also implies that if we change the spatial pump profile  $I_{\text{pump}}(x, y)$  so that it overlaps only with one chosen mode  $\Psi_{\tilde{s}}$ , we get  $A_s = 0$  for  $s \neq \tilde{s}$ , but  $A_{\tilde{s}} \neq 0$ , and the coherence  $g_{\text{total}}^{(1)}$  becomes identical to the coherence  $g_{\tilde{s}}^{(1)}$  of the chosen mode.

---

<sup>1</sup>If the camera which records the interference image has an integration time of  $\Delta t = 1\text{s}$ , this assumption will be true as long as the energy difference between different states is larger than  $\Delta E = \hbar/\Delta t \approx 6.63 \times 10^{-34}\text{J} = 4.14 \times 10^{-15}\text{eV}$ . Even for two modes as defined in equation 8.3 which differ only by the sign of  $m_s$ , under real experimental conditions there will always be a sufficient symmetry breaking which causes an energy difference of more than this  $\Delta E$ .

<sup>2</sup>Of course in the two-dimensional system, the mode can not be perfectly coherent (chapter 3), but for a reasonable small system size, the quasi long range order can be very similar to perfect coherence.

## 8.4 Simulated data for top-hat

For the simulation, we choose a few possible modes  $\Psi_s$  and fit the amplitudes  $A_s$  so that  $n_{\text{total}}(x, y)$  is approximately proportional to the top-hat profile  $I_{\text{pump}}(x, y) \propto H(R - \sqrt{x^2 + y^2})$ , as shown in Fig. 8.2.

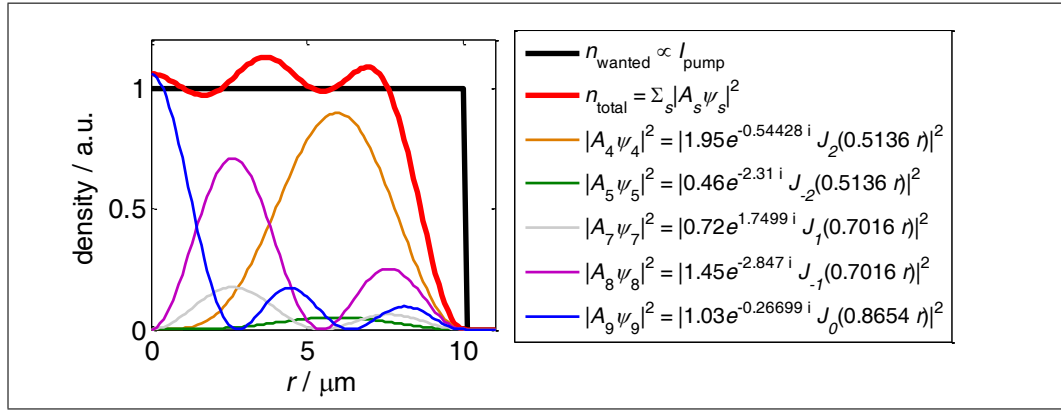


Figure 8.2: Simulated total density  $n_{\text{total}}(x, 0)$  compared to the pump-intensity  $I_{\text{pump}}(x, 0)$ . The contributions  $|A_s \Psi_s(x, 0)|^2$  of the individual modes are also shown.

The simulated Michelson interferometer flips the signal in one arm around the  $y$ -axis, so that photons emitted from the sample at points  $(x, y)$  and  $(-x, y)$  interfere with each other. Even with the assumption of  $g_s^{(1)} \approx 1$  (which is a reasonable approximation since the predicted slow algebraic decay is negligible over the finite condensate size), the simulated  $g_{\text{total}}^{(1)}(x, y, -x, y)$  shows a clear decay (figure 8.4). The simulated interference signal and the simulated interference phase (figure 8.3) show forks [6, 69, 70] in the fringes which look similar to trapped vortices [70], but in our case they are an artifact caused by the simultaneous presence of multiple modes  $\Psi_s$ .

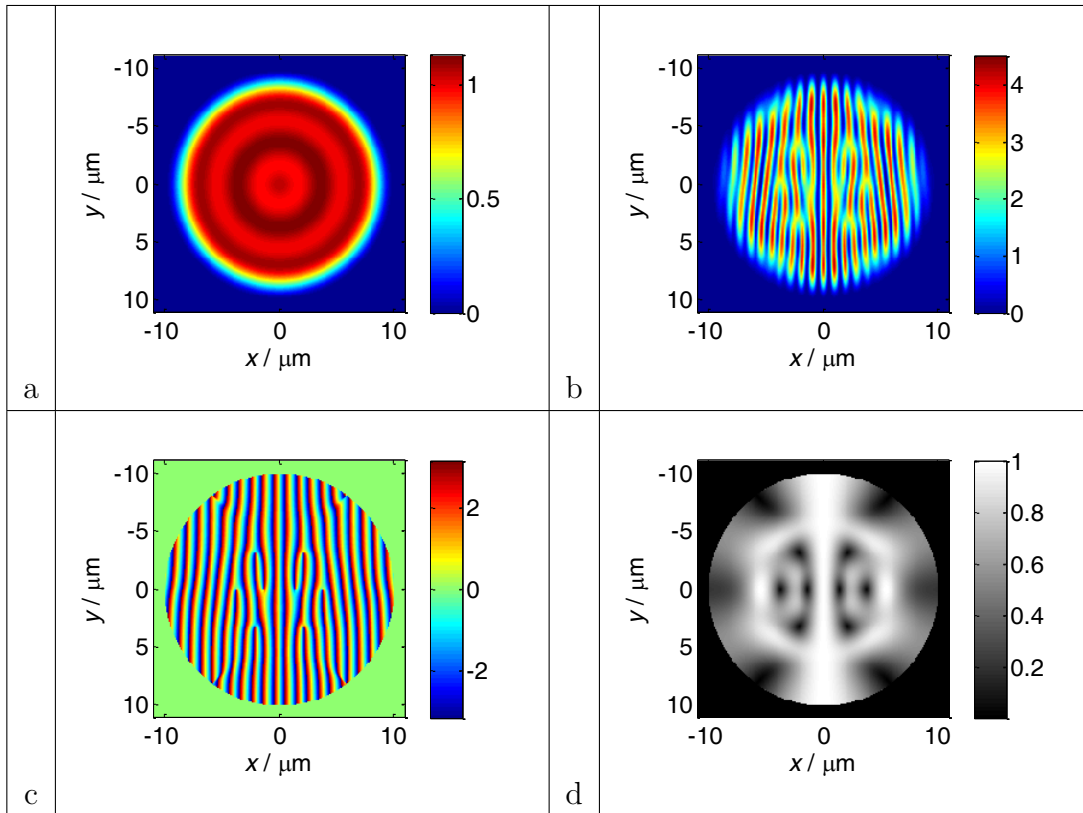


Figure 8.3: Simulated data for top-hat excitation.

(a) Total density  $n_{\text{total}}(x, y)$ .

(b) Interference signal as it would be measured by the camera.

(c) Phase as it would be measured after the interference setup.

(d) Correlation function  $g_{\text{total}}^{(1)}(x, y, -x, y)$ .

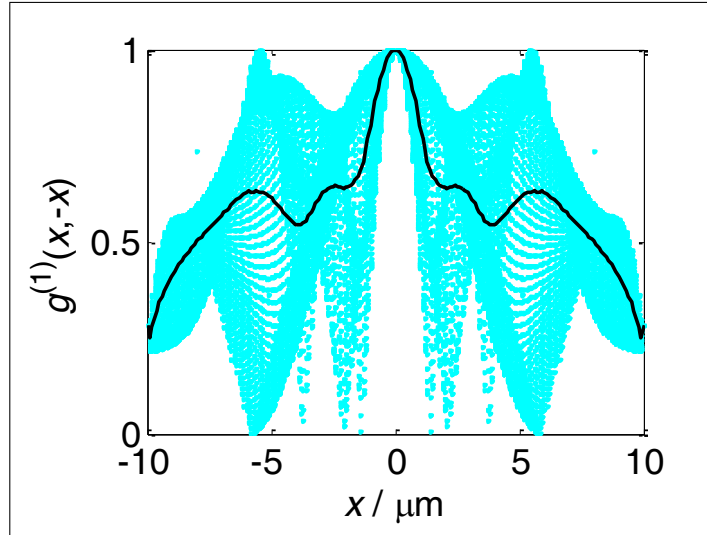


Figure 8.4: All the values of the simulated correlation function in figure 8.3, but plotted as a function of  $x$ . The continuous black line shows the averages of all the data points with the same  $x$ -value. The oscillatory behavior can be understood if we assume that one of the higher modes dominates at larger distances, since the lowest mode is only significant in the region close to the center.

## 8.5 Measured data

Measured data (figures 8.6 and 8.7) show the same behavior as the simulation predicts. The “pseudo-vortices” which are visible as forks in the phase appear even at high temperatures where only VCSEL lasing but no BKT condensation is expected. This confirms that the “pseudo-vortices” are not related to the predicted real vortices in a BKT condensate, but rather they are artifacts from simultaneous emission at different energies  $E_s$ , so that it does not even matter if  $\Psi_s$  represents a BKT condensate or a VCSEL mode. If we slightly move the sample, the “pseudo-vortices” do not move with the sample, but stay at a fixed position relative to the pump-beam. This shows that they cannot be real vortices trapped at defects of the sample.

Chapter 7 showed similar measurements [13] with a Gaussian spatial pump profile,

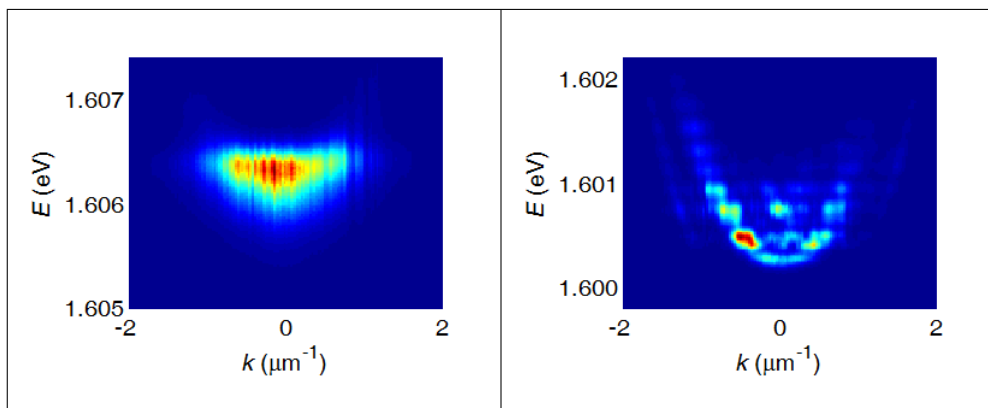


Figure 8.5: Momentum  $k$  and energy  $E$  resolved measurement of the condensate with Gaussian (left) and top-hat (right) excitation. In the top-hat case, it is clearly visible that condensation simultaneously occurs into several fragmented energy levels.

which has only a non-negligible overlap with the lowest mode  $\Psi_1$ . In this case, condensation occurs only into this mode (figure 8.5), and as expected, quasi-long-range order which only decays very slowly has been observed, and no “pseudo-vortices” appeared.

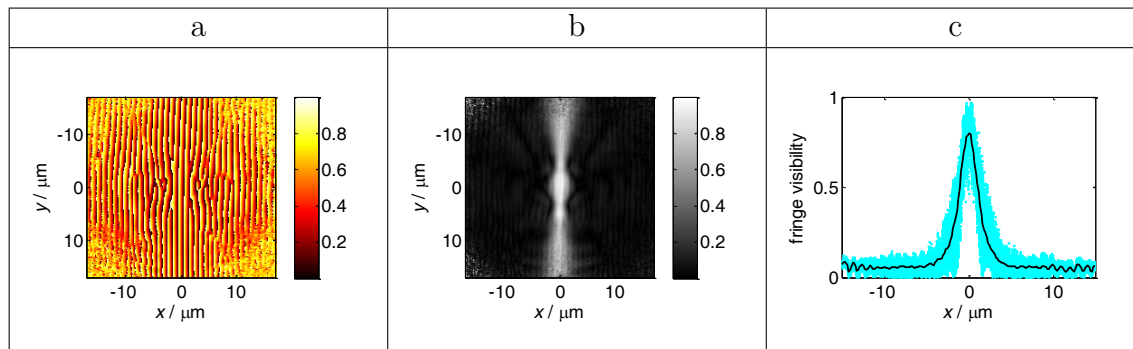


Figure 8.6: Measured (with top-hat excitation) phase (a) and visibility (b,c) at low temperature where the coherence can be explained by condensation. The decay of the visibility is significant faster than measured [13] for a single-mode BKT condensate with quasi-long-range order. The phase shows pseudo-vortices.

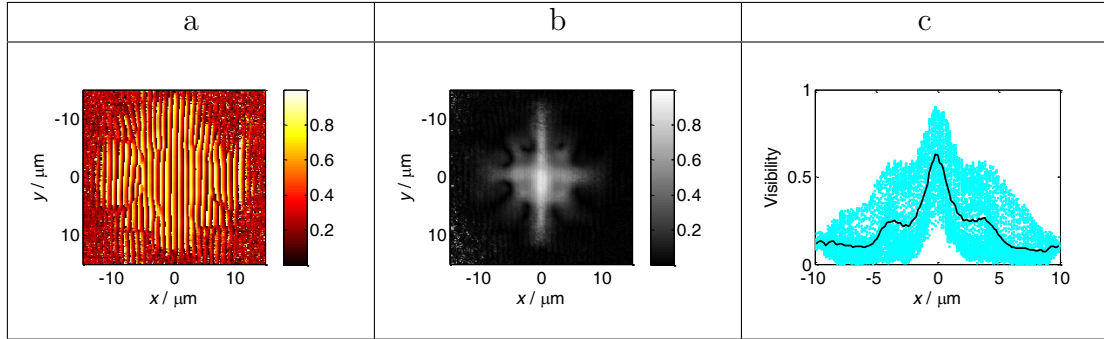


Figure 8.7: Measured (with top-hat excitation) phase (a) and visibility (b,c) at high temperature (200 K) where the coherence can only be explained by VCSEL lasing. Nevertheless, the behavior is the same which confirms that the visibility is determined by the presence of several quantized modes, rather than by the intrinsic coherence properties of a condensate. Pseudo-vortices are visible in the phase map and the visibility shows oscillatory behavior.

## 8.6 Recovery of long range order

If the overall coherence of the system shows fast decay due to the presence of multiple modes, the obvious question is whether it is possible to recover the quasi long-range order by measuring only the coherence of one single mode from the many simultaneously present modes. One possible approach is to use energy filtering. As long as the energy levels of the individual modes are clearly separated and do not overlap, a spectrometer can be used for this filtering. Figure 8.8 shows the modified setup for this measurement. Instead of being recorded by a CCD camera, the (two-dimensional  $x$  and  $y$  resolved) interference image is projected onto the slit of a spectrometer. If the entrance slit of the spectrometer is widely opened, and the grating aligned to act as a mirror ( $0^{\text{th}}$  order), the camera records the position ( $x$  and  $y$ ) resolved image, and the same interference measurement can be done as with the previously used CCD camera. However the spectrometer can also be used to make a position and energy ( $x$  and  $E$ ) resolved measurement. For this, the entrance slit is again closed so that only the signal with  $y \approx 0$  enters the spectrometer, and the grating is aligned in such a

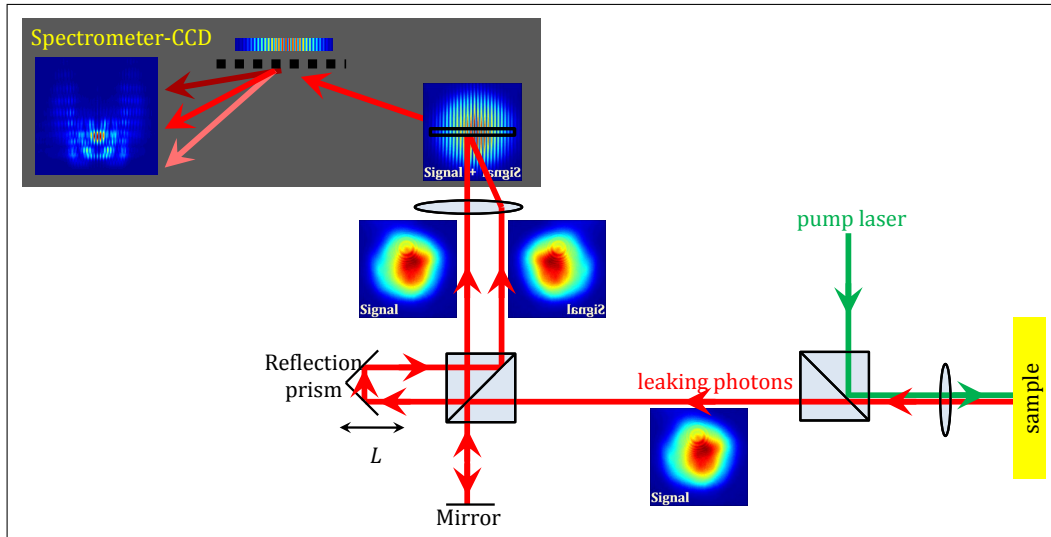


Figure 8.8: Experimental setup for spectrally resolved interference measurement.

way (1<sup>st</sup> order), that the one-dimensional position  $x$  resolved interference signal which passes through the slit becomes spectrally resolved and is recorded as a position and energy ( $x$  and  $E$ ) resolved image.

With this modified setup, the interference measurement has been done both with a  $(x; y)$  and with a  $(x; E)$  resolved measurement under the same experimental conditions (figure 8.9). In the  $x$  and  $E$  resolved case, one can clearly see discrete quantized modes at different energy levels (figures 8.5 and 8.9). In the same way as described in chapter 5, the interference images have been recorded for many different path-length differences and pixelwise evaluated. If one chooses a region of interest in the  $x$  and  $E$  resolved data which includes only one single mode, the measured coherence is significant higher than in the case of the  $x$  and  $y$  resolved data where several modes contribute. This confirms that in the case of a multi-mode condensate, the overall coherence decreases much faster than the intrinsic coherence of each individual mode.

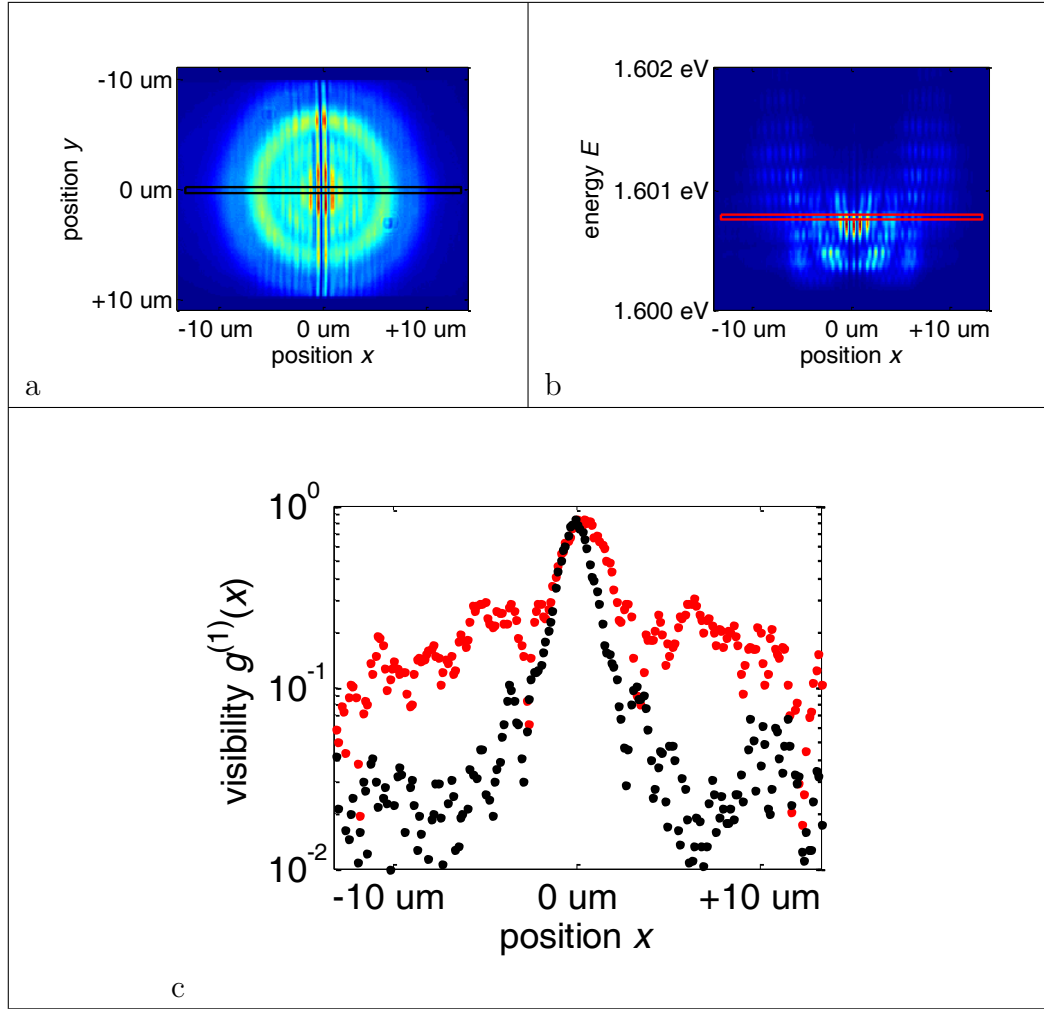


Figure 8.9: Spectrometric resolved interference data with a top-hat pump profile at a temperature of  $T \approx 8\text{K}$  and a detuning of  $\Delta E \approx -8.1\text{meV}$  (far red detuned).

(a) shows a  $x$  and  $y$  resolved interference measurement. The region-of-interest is highlighted by a black rectangle.

(b) shows a position and energy ( $x$  and  $E$ ) resolved interference measurement. The region-of-interest is highlighted by a red rectangle.

(c) shows the visibility from the region-of-interest. Black dots correspond to the data in (a) and red dots to the data in (b). We see that for the energy resolved measurement of one specific mode, the visibility decays slowly, as expected.

## 8.7 Conclusion about fragmented condensates

In conclusion, a BKT condensate with constant spatial density must consist of several modes, the simultaneous presence of which causes a faster than expected decay of the spatial coherence and the appearance of “pseudo-vortices” which look similar to pinned vortices [6–9] or a vortex lattice [70] in a BKT phase. The simultaneous condensation into multiple modes might also explain the previously reported [14] decay of the coherence of an exciton-polariton condensate with a power-law whose exponent is larger than allowed under the BKT theory.

# Chapter 9

## Summary and outlook

This work showed that an exciton-polariton condensate displays the theoretically predicted quasi-long-range order. Since the photons emitted by such a condensate have a high level of coherence, an exciton-polariton condensate in a semiconductor structure could potentially be used as a coherent light source. The widely used vertical cavity surface emitting lasers (VCSELs) require a population inversion, whereas the threshold for exciton-polariton condensation is typically around two orders of magnitude lower [71,72]. Therefore light sources based on the condensation of exciton-polaritons can be used if a lower threshold for the onset of coherent emission is desired.

The main drawbacks for applications of the kind of sample as it has been used for the measurements described in this thesis is the need of liquid helium for cooling, and the need for an additional light source (laser) to pump the sample.

However exciton-polariton condensation has been reported even at room temperature in polymers [22] and large-band-gap semiconductors like GaN [20], which shows that exciton-polariton condensation is possible even without helium cooling.

Recent work [73–76] also demonstrated that an exciton-polariton condensate can be produced by applying a voltage to the sample, which eliminates the need for a pump laser.

Once it becomes possible to build electrically excited samples which allow exciton-polariton condensation at room temperature while maintaining the quasi-long-range order, this might achieve a useful source of coherent light.

# Appendix A

## Visibility and $g^{(1)}$

The measured visibility (as shown in figure 7.3) corresponding to  $(x; y)$  can be calculated as

$$V(x; y) = \frac{2\sqrt{I_1(x; y) I_2(-x; y)}}{I_1(x; y) + I_2(-x; y)} g^{(1)}(x; y, -x; y) \quad (\text{A.1})$$

where  $I_1(x; y)$  is the intensity of the signal which reaches the camera after being emitted from point  $(x; y)$  and travelling through arm 1 of the interferometer and likewise  $I_2$  travels through arm 2. With  $I_1(x; y) = f_1 I(x; y)$  where  $I(x; y)$  is the total emitted intensity at  $(x; y)$  and  $f_1$  is the fraction travelling through arm 1 (and likewise for arm 2), the visibility becomes

$$V(x) = \frac{2\sqrt{f_1 I(x) f_2 I(-x)}}{f_1 I(x) + f_2 I(-x)} g^{(1)}(x, -x) \quad (\text{A.2})$$

where we omitted the constant  $y$ . In theory  $f_1$  and  $f_2$  should be identical, but in reality this usually not the case, for example because the mirror in arm 1 has a different reflectivity than the reflection-prism in arm 2. In our setup, we have  $f_2 \approx 0.80f_1$  which, for  $I(x) = I(-x)$ , as expected for a symmetrical condensate, gives  $V(x) = 0.994g^{(1)}(x, -x)$ , meaning that the differences between  $f_1$  and  $f_2$  can

be neglected. Assuming  $f_1 \approx f_2$  gives

$$V(x) = \frac{2\sqrt{I(x)I(-x)}}{I(x) + I(-x)}g^{(1)}(x, -x) \quad (\text{A.3})$$

which means that the visibility  $V$  will decay faster than  $g^{(1)}$  if  $I(x) \neq I(-x)$  due to an irregular form of the condensate. For a perfectly symmetrical condensate with  $I(x) = I(-x)$ , we get

$$V(x) = g^{(1)}(x, -x) \quad (\text{A.4})$$

which means that under optimal conditions the measured visibility  $V$  is identical to the correlation function  $g^{(1)}$ . As shown in figure 7.5, for pump-powers moderately above condensation threshold, increasing the pump-power decreases the exponent  $a_p$  of the power-law. For even higher pump-powers, the measured  $a_p$  seems to increase, instead of showing the expected steady decrease. This increase can be explained as

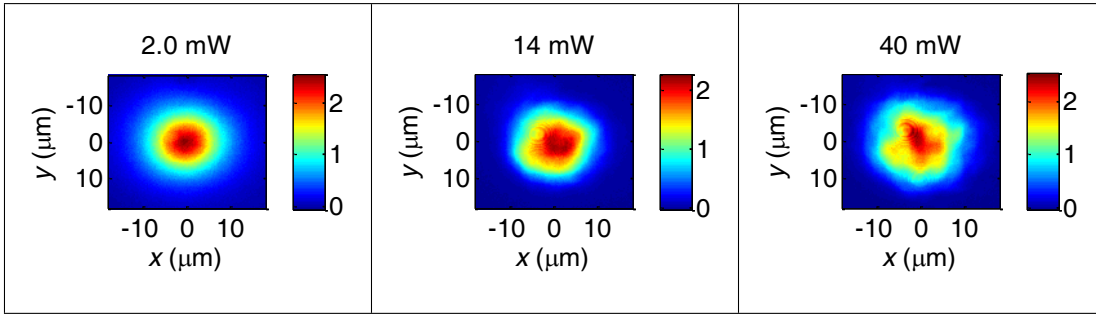


Figure A.1: Pump-power dependent density distribution. The irregular density profile at very high pump-powers prevents us from extracting the exponent  $a_p$  in the very high-power regime (measured at  $\delta \approx -1$  meV).

an artifact resulting from the spatial density of the condensate, which at high pump-powers deviates from a Gaussian profile and becomes increasingly non-symmetric (Fig. A.1) so that  $I(x) \neq I(-x)$ , which causes the measured visibility to decay faster than  $g^{(1)}$ . Therefore, for figures 7.5 (upper row) and 7.7, we did not consider data from very high pump-powers corresponding to an irregular condensate form.

We believe that the irregularities [32] of the condensate form are caused by local fluctuations of the sample properties. In the case of irregular condensate forms, we see certain patterns like dark lines going through the condensate, and if we slightly move the sample, these patterns move with the sample, which indicates that they are caused by local properties of the sample. In theory, the visibility is always expected to be symmetrical, so that  $V(x) = V(-x)$ . However equation A.2 shows that under realistic experimental conditions,  $V(x) \neq V(-x)$  is possible if  $I(x) \neq I(-x)$  and at the same time  $f_1 \neq f_2$ . This can explain the slightly asymmetric data in figure 7.3 (c). [13]



# Appendix B

## Simulated fast visibility decay

To demonstrate that the fast decay in region III of figure 7.3 (c) can be explained by a decreasing superfluid fraction  $n_s/n$  at the edge of the condensate, we simulated the visibility (figure B.1). For this, we assumed a condensate with a radius of  $15 \mu\text{m}$ ,

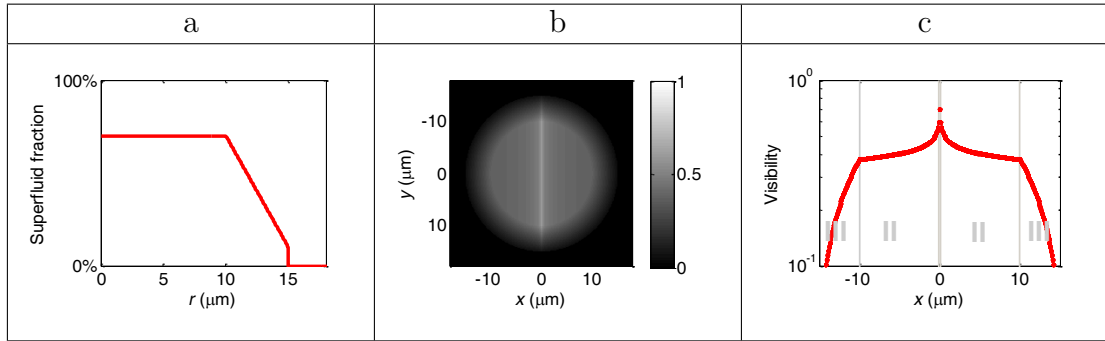


Figure B.1: Simulated visibility.

- (a) Assumed position dependent superfluid fraction as a function of radial position  $r$ .
- (b) Simulated visibility assuming  $g^{(1)} = (n_s/n) (|x|/0.02 \mu\text{m})^{-0.1}$ .
- (c) Simulated visibility at  $y \approx 0$ . The simulated fast decay in region III shows that the fast decay in figure 7.3 (c) can be explained by a decreasing superfluid fraction.

where the superfluid fraction is constant for  $r < 10 \mu\text{m}$  and slowly decreases to a small value at  $r = 15 \mu\text{m}$ , where it jumps to 0 %. [13]



# Appendix C

## Simulated power-law

The theory for the BKT phase predicts that the power-law decay of the correlation function  $g^{(1)}$  is the result of thermally excited phonon modes whereas all vortices are paired so that they cannot affect  $g^{(1)}$ . We simulated a two-dimensional condensate whose phase fluctuations are caused by phonons with wavelengths of at least  $2\pi$  times the healing length (figure C.1). For this simulation [13], we assumed that the number of phonons in the different possible modes follow a phonon statistic, meaning that the probability to have exactly  $N_{\mathbf{k}}$  phonons in the mode  $\mathbf{k}$  is

$$p_{N_{\mathbf{k}}} = \frac{\exp\left(-\frac{N_{\mathbf{k}}\varepsilon_{\mathbf{k}}}{k_{\text{B}}T}\right)}{1 - \exp\left(-\frac{\varepsilon_{\mathbf{k}}}{k_{\text{B}}T}\right)} \quad (\text{C.1})$$

where  $\varepsilon_{\mathbf{k}} = \hbar c |\mathbf{k}|$  is the energy per phonon in this mode  $\mathbf{k}$ . The local phase can be expressed [42] in the form  $\Theta(\mathbf{r}) = \alpha_{\mathbf{k}} \sin(\mathbf{k}\mathbf{r} + \varphi_{\mathbf{k}})$  where the Fourier amplitudes  $\alpha_{\mathbf{k}}$  depend on the numbers  $N_{\mathbf{k}}$  of phonons in the respective modes. No vortices have been considered in this simulation. As expected, the simulated visibility decays with a power-law, which confirms that this characteristic decay can be caused by thermally excited phonons, rather than by the presence of vortices. The same result can also be derived [42] analytically.

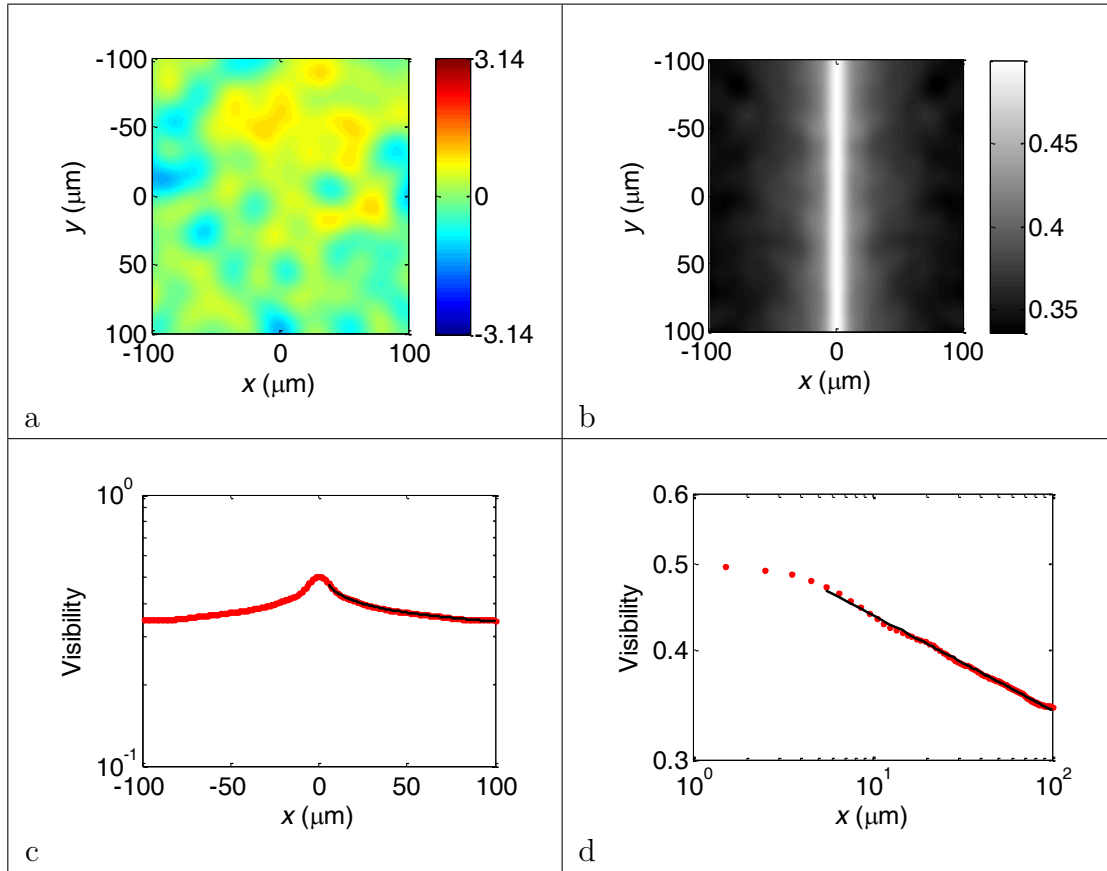


Figure C.1: Simulated power-law.

(a) Phase  $\Theta$  in one run of the simulation.

(b, c) Visibility averaged over 1000 runs of the simulation.

(d) The same visibility shown as a log-log plot where the power-law appears as a straight line.

# Appendix D

## Transition from power-law to faster decay

In figure 7.3 (c), we see that the power-law (II) ends at a “cut-off”-length beyond which a much faster decay (III) is observed. This data has been extracted close to  $y = 0$  in figure 7.3 (b). By performing the same evaluation for different  $y$ -values, we see that the “cut-off”-points seem to lie on a circle (figure D.1), which confirms our interpretation that the fast decay of the visibility is caused by a decrease of the condensation-fraction towards the edge of the condensate. [13]

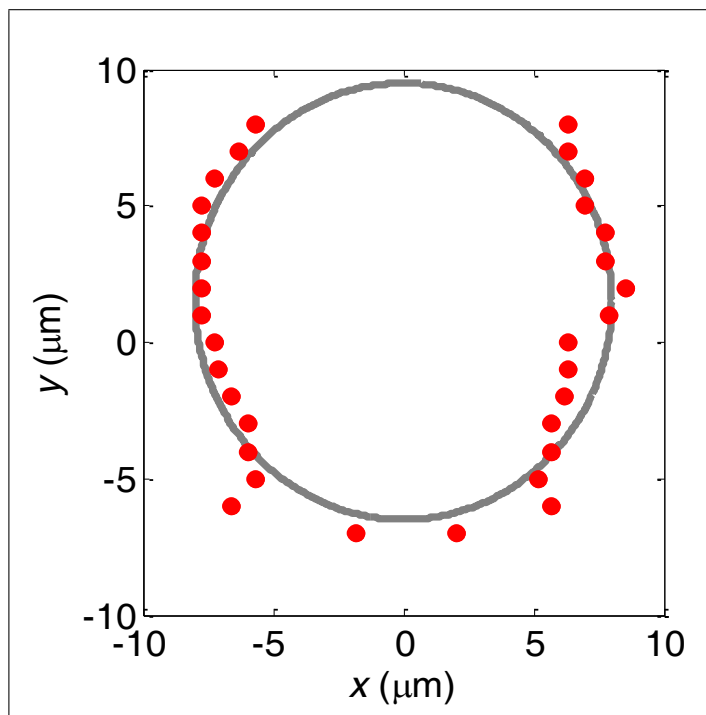


Figure D.1: Transition from power law to fast decay of visibility. The red points show the measured “cut-off”-points where the power-law ends. They seem to form a circle which corresponds to the rotational symmetry of the Gaussian pump beam.

# Appendix E

## Measured visibilities at different conditions

Figures E.1 and E.2 show measured visibilities, similar to figure 7.3 (c), but for different pump-powers and detuning values. One can see the existence of quasi-long-range order above condensation threshold, but only Gaussian decay below condensation threshold.

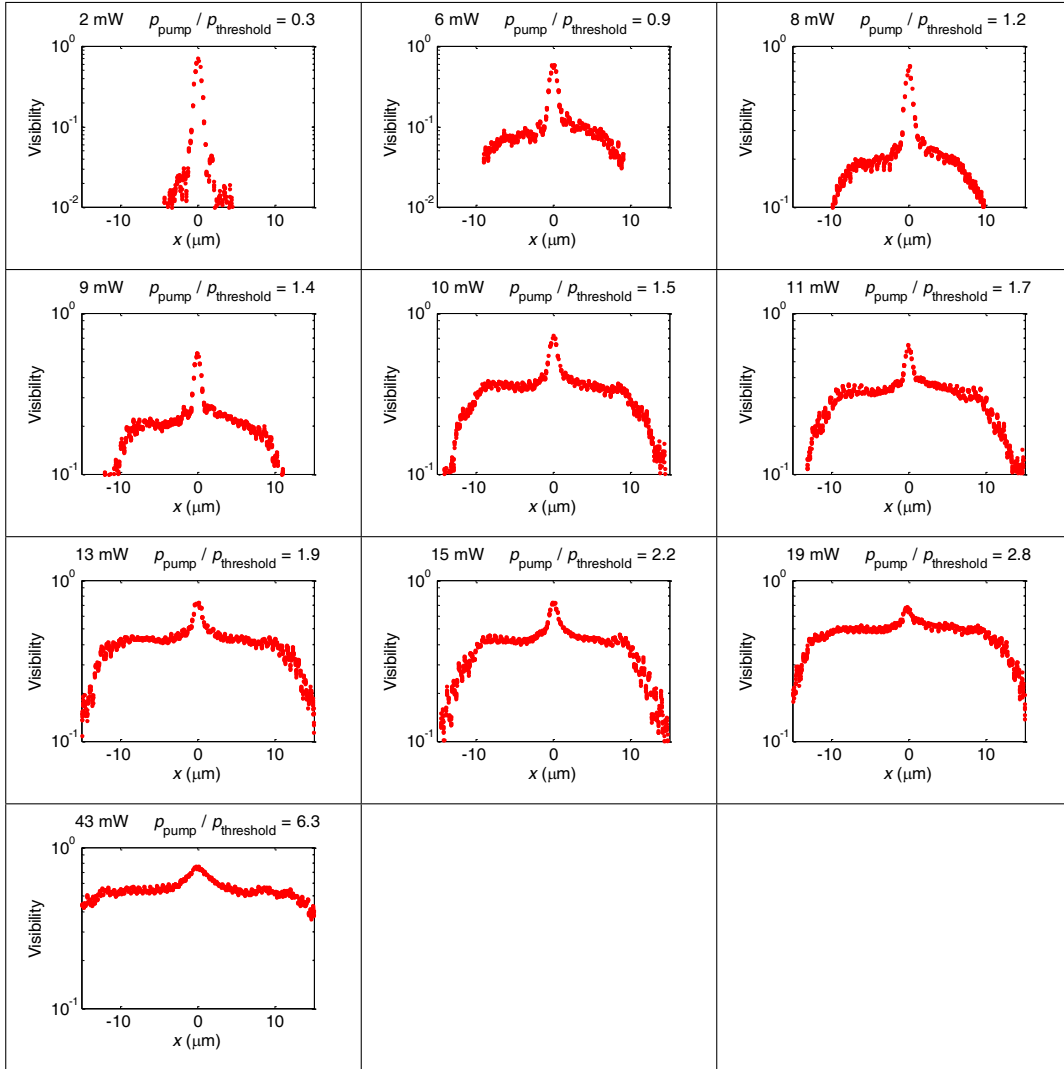


Figure E.1: Measured visibility at a detuning of -1 meV.

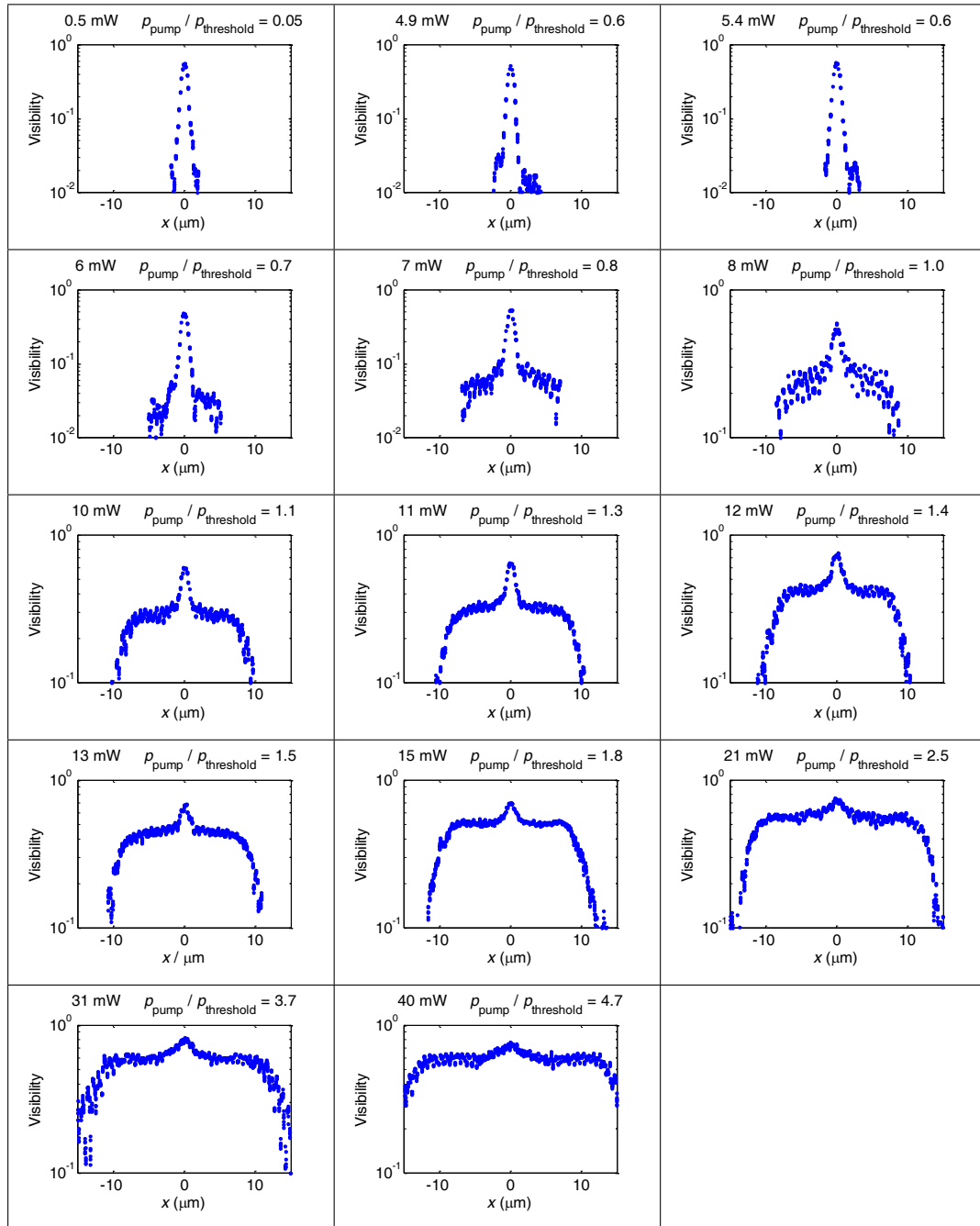


Figure E.2: Measured visibility at a detuning of 4 meV.



# Bibliography

- [1] C. Weisbuch, M. Nishioka, A. Ishikawa, and Y. Arakawa. Observation of the coupled exciton-photon mode splitting in a semiconductor quantum microcavity. *Physical Review Letters*, 69:3314–3317, December 1992.
- [2] M. S. Skolnick, T. A. Fisher, and D. M. Whittaker. Topical review: Strong coupling phenomena in quantum microcavity structures. *Semiconductor Science Technology*, 13:645–669, July 1998.
- [3] H. Deng, G. Weihs, C. Santori, J. Bloch, and Y. Yamamoto. Condensation of semiconductor microcavity exciton polaritons. *Science*, 298:199–202, October 2002.
- [4] J. Kasprzak, M. Richard, S. Kundermann, A. Baas, P. Jeambrun, J. M. J. Keeling, F. M. Marchetti, M. H. Szymańska, R. André, J. L. Staehli, V. Savona, P. B. Littlewood, B. Deveaud, and L. S. Dang. Bose-Einstein condensation of exciton polaritons. *Nature*, 443:409–414, September 2006.
- [5] G. Roumpos, M. D. Fraser, A. Löffler, S. Höfling, A. Forchel, and Y. Yamamoto. Single vortex-antivortex pair in an exciton-polariton condensate. *Nature Physics*, 7:129–133, February 2011.

- [6] K. G. Lagoudakis, M. Wouters, M. Richard, A. Baas, I. Carusotto, R. André, L. S. Dang, and B. Deveaud-Plédran. Quantized vortices in an exciton-polariton condensate. *Nature Physics*, 4:706, September 2008.
- [7] K. G. Lagoudakis, T. Ostatnický, A. V. Kavokin, Y. G. Rubo, R. André, and B. Deveaud-Plédran. Observation of half-quantum vortices in an exciton-polariton condensate. *Science*, 326:974–976, November 2009.
- [8] F. M. Marchetti, M. H. Szymańska, C. Tejedor, and D. M. Whittaker. Spontaneous and triggered vortices in polariton optical-parametric-oscillator superfluids. *Physical Review Letters*, 105:063902, August 2010.
- [9] K. G. Lagoudakis, F. Manni, B. Pietka, M. Wouters, T. C. H. Liew, V. Savona, A. V. Kavokin, R. André, and B. Deveaud-Plédran. Probing the dynamics of spontaneous quantum vortices in polariton superfluids. *Physical Review Letters*, 106:115301, March 2011.
- [10] V. Savona, F. Tassone, C. Piermarocchi, A. Quattropani, and P. Schwendimann. Theory of polariton photoluminescence in arbitrary semiconductor microcavity structures. *Physical Review B*, 53:13051–13062, May 1996.
- [11] S. Utsunomiya, L. Tian, G. Roumpos, C. W. Lai, N. Kumada, T. Fujisawa, M. Kuwata-Gonokami, A. Löffler, S. Höfling, A. Forchel, and Y. Yamamoto. Observation of Bogoliubov excitations in exciton-polariton condensates. *Nature Physics*, 4:700–705, September 2008.
- [12] Wolfgang H. Nitsche, Na Young Kim, Georgios Roumpos, Sven Höfling, Alfred Forchel, and Yoshihisa Yamamoto. Observation of BKT transition in BEC of exciton-polaritons in a semiconductor microcavity. In *CLEO: 2013*, page QM1D.3. Optical Society of America, 2013.

- [13] W. H. Nitsche, N. Y. Kim, G. Roumpos, C. Schneider, M. Kamp, S. Höfling, A. Forchel, and Y. Yamamoto. Algebraic order and the Berezinskii-Kosterlitz-Thouless transition in an exciton-polariton gas. *ArXiv*, 1401.0756, January 2014.
- [14] G. Roumpos, M. Lohse, W. H. Nitsche, J. Keeling, M. H. Szymańska, P. B. Littlewood, A. Löffler, S. Höfling, L. Worschech, A. Forchel, and Y. Yamamoto. Power-law decay of the spatial correlation function in exciton-polariton condensates. *Proceedings of the National Academy of Science*, 109:6467–6472, April 2012.
- [15] H. Deng, H. Haug, and Y. Yamamoto. Exciton-polariton Bose-Einstein condensation. *Reviews of Modern Physics*, 82:1489–1537, April 2010.
- [16] R. Balili, V. Hartwell, D. Snoke, L. Pfeiffer, and K. West. Bose-Einstein condensation of microcavity polaritons in a trap. *Science*, 316:1007–1010, May 2007.
- [17] D. M. Whittaker, P. Kinsler, T. A. Fisher, M. S. Skolnick, A. Armitage, A. M. Afshar, M. D. Sturge, and J. S. Roberts. Motional narrowing in semiconductor microcavities. *Physical Review Letters*, 77:4792–4795, December 1996.
- [18] H. Deng, D. Press, S. Götzinger, G. S. Solomon, R. Hey, K. H. Ploog, and Y. Yamamoto. Quantum degenerate exciton-polaritons in thermal equilibrium. *Physical Review Letters*, 97:146402, October 2006.
- [19] S. Kéna-Cohen and S. R. Forrest. Room-temperature polariton lasing in an organic single-crystal microcavity. *Nature Photonics*, 4:371–375, June 2010.
- [20] S. Christopoulos, G. Baldassarri Höger von Högersthal, A. J. D. Grundy, P. G. Lagoudakis, A. V. Kavokin, J. J. Baumberg, G. Christmann, R. Butté, E. Feltn, J.-F. Carlin, and N. Grandjean. Room-temperature polariton lasing in semiconductor microcavities. *Physical Review Letters*, 98:126405, Mar 2007.

- [21] J. J. Baumberg, A. V. Kavokin, S. Christopoulos, A. J. D. Grundy, R. Butté, G. Christmann, D. D. Solnyshkov, G. Malpuech, G. Baldassarri Höger von Högersthal, E. Feltin, J.-F. Carlin, and N. Grandjean. Spontaneous polarization buildup in a room-temperature polariton laser. *Physical Review Letters*, 101:136409, September 2008.
- [22] J. D. Plumhof, T. Stöferle, L. Mai, U. Scherf, and R. F. Mahrt. Room-temperature Bose-Einstein condensation of cavity exciton-polaritons in a polymer. *Nature Materials*, 13:247–252, March 2014.
- [23] M. H. Anderson, J. R. Ensher, M. R. Matthews, C. E. Wieman, and E. A. Cornell. Observation of Bose-Einstein condensation in a dilute atomic vapor. *Science*, 269:198–201, July 1995.
- [24] D. Bajoni, P. Senellart, E. Wertz, I. Sagnes, A. Miard, A. Lemaître, and J. Bloch. Polariton laser using single micropillar GaAs-GaAlAs semiconductor cavities. *Physical Review Letters*, 100:047401, February 2008.
- [25] E. Wertz, L. Ferrier, D. D. Solnyshkov, R. Johne, D. Sanvitto, A. Lemaître, I. Sagnes, R. Grousson, A. V. Kavokin, P. Senellart, G. Malpuech, and J. Bloch. Spontaneous formation and optical manipulation of extended polariton condensates. *Nature Physics*, 6:860–864, November 2010.
- [26] P. G. Savvidis, J. J. Baumberg, R. M. Stevenson, M. S. Skolnick, D. M. Whittaker, and J. S. Roberts. Angle-resonant stimulated polariton amplifier. *Physical Review Letters*, 84:1547–1550, February 2000.
- [27] R. Huang, F. Tassone, and Y. Yamamoto. Experimental evidence of stimulated scattering of excitons into microcavity polaritons. *Physical Review B*, 61:7854, March 2000.

- [28] M. Wouters and I. Carusotto. Excitations in a nonequilibrium Bose-Einstein condensate of exciton polaritons. *Physical Review Letters*, 99:140402, October 2007.
- [29] D. Porras, C. Ciuti, J. J. Baumberg, and C. Tejedor. Polariton dynamics and Bose-Einstein condensation in semiconductor microcavities. *Physical Review B*, 66:085304, Aug 2002.
- [30] L.D. Landau and E.M. Lifshitz. *Fluid Mechanics*. Number 6. Pergamon Press, 1959.
- [31] A. Amo, S. Pigeon, D. Sanvitto, V. G. Sala, R. Hivet, I. Carusotto, F. Pisanello, G. Leménager, R. Houdré, E. Giacobino, C. Ciuti, and A. Bramati. Polariton superfluids reveal quantum hydrodynamic solitons. *Science*, 332:1167–1170, June 2011.
- [32] A. Amo, J. Lefrère, S. Pigeon, C. Adrados, C. Ciuti, I. Carusotto, R. Houdré, E. Giacobino, and A. Bramati. Superfluidity of polaritons in semiconductor microcavities. *Nature Physics*, 5:805–810, November 2009.
- [33] A. Kavokin, J.J. Baumberg, G. Malpuech, and F.P. Laussy. *Microcavities*. Oxford science publications. OUP Oxford, 2011.
- [34] R. Ozeri, N. Katz, J. Steinhauer, and N. Davidson. Colloquium: Bulk Bogoliubov excitations in a Bose-Einstein condensate. *Reviews of Modern Physics*, 77:187–205, January 2005.
- [35] M. W. Zwierlein, J. R. Abo-Shaeer, A. Schirotzek, C. H. Schunck, and W. Ketterle. Vortices and superfluidity in a strongly interacting Fermi gas. *Nature*, 435:1047–1051, June 2005.

- [36] I. Bloch, T. W. Hänsch, and T. Esslinger. Measurement of the spatial coherence of a trapped Bose gas at the phase transition. *Nature*, 403:166–170, January 2000.
- [37] N. D. Mermin and H. Wagner. Absence of ferromagnetism or antiferromagnetism in one- or two-dimensional isotropic Heisenberg models. *Physical Review Letters*, 17:1133–1136, November 1966.
- [38] P. C. Hohenberg. Existence of long-range order in one and two dimensions. *Physical Review*, 158:383–386, June 1967.
- [39] Z. Hadzibabic, P. Krüger, M. Cheneau, S. P. Rath, and J. Dalibard. The trapped two-dimensional Bose gas: from Bose-Einstein condensation to Berezinskii-Kosterlitz-Thouless physics. *New Journal of Physics*, 10:045006, April 2008.
- [40] V. L. Berezinskiĭ. Destruction of long-range order in one-dimensional and two-dimensional systems possessing a continuous symmetry group. II. Quantum systems. *Soviet Journal of Experimental and Theoretical Physics*, 34:610–616, March 1972.
- [41] J. M. Kosterlitz and D. J. Thouless. Ordering, metastability and phase transitions in two-dimensional systems. *Journal of Physics C Solid State Physics*, 6:1181–1203, April 1973.
- [42] Z. Hadzibabic and J. Dalibard. Two-dimensional Bose fluids: An atomic physics perspective. *Rivista del Nuovo Cimento*, 34:389–433, 2011.
- [43] Z. Hadzibabic, P. Krüger, M. Cheneau, B. Battelier, and J. Dalibard. Berezinskii-Kosterlitz-Thouless crossover in a trapped atomic gas. *Nature*, 441:1118–1121, June 2006.

- [44] J.-y. Choi, S. W. Seo, and Y.-i. Shin. Observation of thermally activated vortex pairs in a quasi-2D bose gas. *Physical Review Letters*, 110:175302, April 2013.
- [45] M. D. Fraser, G. Roumpos, and Y. Yamamoto. Vortex-antivortex pair dynamics in an exciton-polariton condensate. *New Journal of Physics*, 11:113048, November 2009.
- [46] M. H. Szymańska, J. Keeling, and P. B. Littlewood. Mean-field theory and fluctuation spectrum of a pumped decaying Bose-Fermi system across the quantum condensation transition. *Physical Review B*, 75:195331, May 2007.
- [47] J. V. José, L. P. Kadanoff, S. Kirkpatrick, and D. R. Nelson. Renormalization, vortices, and symmetry-breaking perturbations in the two-dimensional planar model. *Physical Review B*, 16:1217–1241, August 1977.
- [48] D. R. Nelson and J. M. Kosterlitz. Universal jump in the superfluid density of two-dimensional superfluids. *Physical Review Letters*, 39:1201–1205, November 1977.
- [49] J. Bloch, T. Freixanet, J. Y. Marzin, V. Thierry-Mieg, and R. Planel. Giant Rabi splitting in a microcavity containing distributed quantum wells. *Applied Physics Letters*, 73:1694–1696, 1998.
- [50] M. Saba, C. Ciuti, J. Bloch, V. Thierry-Mieg, R. André, L. S. Dang, S. Kundermann, A. Mura, G. Bongiovanni, J. L. Staehli, and B. Deveaud. High-temperature ultrafast polariton parametric amplification in semiconductor microcavities. *Nature*, 414:731–735, December 2001.
- [51] F. Tassone, F. Bassani, and L. C. Andreani. Quantum-well reflectivity and exciton-polariton dispersion. *Physical Review B*, 45:6023–6030, March 1992.

- [52] C. W. Lai, N. Y. Kim, S. Utsunomiya, G. Roumpos, H. Deng, M. D. Fraser, T. Byrnes, P. Recher, N. Kumada, T. Fujisawa, and Y. Yamamoto. Coherent zero-state and  $\pi$ -state in an exciton-polariton condensate array. *Nature*, 450:529–532, November 2007.
- [53] K. B. Davis, M.-O. Mewes, M. R. Andrews, N. J. van Druten, D. S. Durfee, D. M. Kurn, and W. Ketterle. Bose-Einstein condensation in a gas of sodium atoms. *Physical Review Letters*, 75:3969–3973, November 1995.
- [54] P. Kaapitza. Viscosity of liquid helium below the  $\lambda$ -point. *Nature*, 141:74, January 1938.
- [55] A. Amo, D. Sanvitto, F. P. Laussy, D. Ballarini, E. D. Valle, M. D. Martin, A. Lemaître, J. Bloch, D. N. Krizhanovskii, M. S. Skolnick, C. Tejedor, and L. Viña. Collective fluid dynamics of a polariton condensate in a semiconductor microcavity. *Nature*, 457:291–295, January 2009.
- [56] D. Sanvitto, F. M. Marchetti, M. H. Szymańska, G. Tosi, M. Baudisch, F. P. Laussy, D. N. Krizhanovskii, M. S. Skolnick, L. Marrucci, A. Lemaître, J. Bloch, C. Tejedor, and L. Viña. Persistent currents and quantized vortices in a polariton superfluid. *Nature Physics*, 6:527–533, July 2010.
- [57] H. Deng, G. S. Solomon, R. Hey, K. H. Ploog, and Y. Yamamoto. Spatial coherence of a polariton condensate. *Physical Review Letters*, 99:126403, September 2007.
- [58] F. Manni, K. G. Lagoudakis, B. Pietka, L. Fontanesi, M. Wouters, V. Savona, R. André, and B. Deveaud-Plédran. Polariton condensation in a one-dimensional disordered potential. *Physical Review Letters*, 106:176401, April 2011.

- [59] O. Tsypliyatyev and D. M. Whittaker. Spatial coherence of a polariton condensate in 1D acoustic lattice. *Physica Status Solidi B Basic Research*, 249:1692–1697, September 2012.
- [60] A. Trichet, E. Durupt, F. Médard, S. Datta, A. Minguzzi, and M. Richard. Long-range correlations in a 97% excitonic one-dimensional polariton condensate. *Physical Review B*, 88:121407, September 2013.
- [61] D. J. Bishop and J. D. Reppy. Study of the superfluid transition in two-dimensional  $^4\text{He}$  films. *Physical Review Letters*, 40:1727–1730, June 1978.
- [62] D. J. Bishop and J. D. Reppy. Study of the superfluid transition in two-dimensional  $^4\text{He}$  films. *Physical Review B*, 22:5171–5185, December 1980.
- [63] M. R. Beasley, J. E. Mooij, and T. P. Orlando. Possibility of vortex-antivortex pair dissociation in two-dimensional superconductors. *Physical Review Letters*, 42:1165–1168, April 1979.
- [64] A. F. Hebard and A. T. Fiory. Evidence for the Kosterlitz-Thouless transition in thin superconducting aluminum films. *Physical Review Letters*, 44:291–294, January 1980.
- [65] E. Altman, L. M. Sieberer, L. Chen, S. Diehl, and J. Toner. Two-dimensional superfluidity of exciton-polaritons requires strong anisotropy. *ArXiv*, 1311.0876, November 2013.
- [66] G. Roumpos, W. H. Nitsche, S. Höfling, A. Forchel, and Y. Yamamoto. Gain-induced trapping of microcavity exciton polariton condensates. *Physical Review Letters*, 104:126403, March 2010.

- [67] G. Roumpos, C.-W. Lai, T. C. H. Liew, Y. G. Rubo, A. V. Kavokin, and Y. Yamamoto. Signature of the microcavity exciton-polariton relaxation mechanism in the polarization of emitted light. *Physical Review B*, 79:195310, May 2009.
- [68] D. N. Krizhanovskii, K. G. Lagoudakis, M. Wouters, B. Pietka, R. A. Bradley, K. Guda, D. M. Whittaker, M. S. Skolnick, B. Deveaud-Plédran, M. Richard, R. André, and L. S. Dang. Coexisting nonequilibrium condensates with long-range spatial coherence in semiconductor microcavities. *Physical Review B*, 80:045317, July 2009.
- [69] M. Wouters and V. Savona. Creation and detection of vortices in polariton condensates. *ArXiv*, 0904.2966, April 2009.
- [70] F. Manni, T. C. H. Liew, K. G. Lagoudakis, C. Ouellet-Plamondon, R. André, V. Savona, and B. Deveaud. Spontaneous self-ordered states of vortex-antivortex pairs in a polariton condensate. *Physical Review B*, 88:201303, November 2013.
- [71] H. Deng, G. Weihs, D. Snoke, J. Bloch, and Y. Yamamoto. Polariton lasing vs. photon lasing in a semiconductor microcavity. *Proceedings of the National Academy of Science*, 100:15318–15323, December 2003.
- [72] P. Tsotsis, P. S. Eldridge, T. Gao, S. I. Tsintzos, Z. Hatzopoulos, and P. G. Savvidis. Lasing threshold doubling at the crossover from strong to weak coupling regime in GaAs microcavity. *New Journal of Physics*, 14:023060, February 2012.
- [73] C. Schneider, N. Y. Kim, A. Rahimi-Iman, W. H. Nitsche, M. Lermer, M. Kamp, S. Reitzenstein, L. Worschech, S. Höfling, Y. Yamamoto, and A. Forchel. Exciton-polariton laser diodes. In *Semiconductor Laser Conference (ISLC), 2010 22nd IEEE International*, pages 201–202, Sept 2010.

- [74] C. Schneider, A. Rahimi-Iman, N. Y. Kim, J. Fischer, I. G. Savenko, M. Amthor, M. Lermer, A. Wolf, L. Worschech, V. D. Kulakovskii, I. A. Shelykh, M. Kamp, S. Reitzenstein, A. Forchel, Y. Yamamoto, and S. Höfling. An electrically pumped polariton laser. *Nature*, 497:348–352, May 2013.
- [75] P. Bhattacharya, B. Xiao, A. Das, S. Bhowmick, and J. Heo. Solid state electrically injected exciton-polariton laser. *Physical Review Letters*, 110:206403, May 2013.
- [76] D. Solnyshkov, E. Petrolati, A. di Carlo, and G. Malpuech. Theory of an electrically injected bulk polariton laser. *Applied Physics Letters*, 94:011110, January 2009.